PHYSICAL SCIENCES

Power-integrated, wireless neural recording systems on the cranium using a direct printing method for deep-brain analysis

Yong Won Kwon[1,2]†, David B. Ahn[3]†, Young-Geun Park[1,2]†, Enji Kim[1,2], Dong Ha Lee[1,2], Sang-Woo Kim[3], Kwon-Hyung Lee[4], Won-Yeong Kim[5], Yeon-Mi Hong[1,2], Chin Su Koh[6], Hyun Ho Jung[6], Jin Woo Chang[7], Sang-Young Lee[5]*, Jang-Ung Park[1,2,6,8]*

Conventional power-integrated wireless neural recording devices suffer from bulky, rigid batteries in head-mounted configurations, hindering the precise interpretation of the subject's natural behaviors. These power sources also pose risks of material leakage and overheating. We present the direct printing of a power-integrated wireless neural recording system that seamlessly conforms to the cranium. A quasi–solid-state Zn-ion microbattery was 3D-printed as a built-in power source geometrically synchronized to the shape of a mouse skull. Soft deep-brain neural probes, interconnections, and auxiliary electronics were also printed using liquid metals on the cranium with high resolutions. In vivo studies using mice demonstrated the reliability and biocompatibility of this wireless neural recording system, enabling the monitoring of neural activities across extensive brain regions without notable heat generation. This all-printed neural interface system revolutionizes brain research, providing bioconformable, customizable configurations for improved data quality and naturalistic experimentation.

INTRODUCTION

The brain constitutes an intricate three-dimensional (3D) network composed of an immense number of neurons continually generating and transmitting signals for communication. These neuronal activities and firing patterns play a pivotal role in governing bodily functions, consciousness, and the formation of memories. Comprehending the electrophysiology of neurons and functional connectivity of network-level neuronal activities is essential for fundamental research in the treatment of numerous neurological diseases, such as Parkinson's disease (PD), Alzheimer's disease, epilepsy, and major depressive disorder (*1*). In response to the challenge, implantable electronic devices known as neural probes have seen notable development. These devices are designed to convert neural signals into electronic signals, allowing for the precise monitoring of neuronal activities within specific brain regions (*2*–*6*). In particular, recent advances in microfabrication technologies and bioelectronics have enabled flexible neural probes for reliable recording by ensuring mechanical and structural compatibility with brain tissues (*7*–*12*).

A predominant perspective in neuroscience and biomedical engineering is that the activities of a neuronal population are notably influenced by the state of the subject. This perspective allows for a better understanding of neuronal computations related to diverse behavioral and cognitive processes, particularly during unrestricted movement and freely movable states (*13*, *14*). However, the use of numerous neural probes connected to external recording devices via cables and wires limits the subject's freedom of movement. Consequently, wireless neural recording devices have become indispensable to facilitate more natural movements and behaviors in subjects. This is especially crucial in studies aiming to comprehend how the brain responds to specific environments and tasks. In addition, wireless neural recording holds the potential to enhance data quality by eliminating the possibility of noise and interference caused by wires (*15*–*23*).

Considering the substantial amount of neural data to be collected, the most applicable technology for wireless neural recording is a battery-powered system with widespread availability of the associated hardware (*18*, *20*–*22*). Batteries, known for their high energy density and operational stability, make them a promising choice for powering neural interface devices. However, current bulky and rigid battery configurations occupy over 90% of the device volume and more than 60% of its mass (*16*). To use these batteries on small animals, additional fixtures or suits are required to attach them to the head or back, hindering the free behavior of experimental animals (*24*, *25*). Moreover, the risk of electrolyte leakage and overheating in conventional batteries poses a substantial obstacle to the formation of bio-integrated systems (*26*–*29*). Therefore, there is a strong need for batteries that (i) can be shaped to conform to nonplanar biological surfaces and (ii) consist of quasi–solid-state, biocompatible electrolytes to prevent leaks in wireless neural interfaces.

In considering the entire neural interface system, various auxiliary electronic components are essential for the collection and processing of raw signals detected by neural probes. While numerous efforts have been made to enhance the long-term stability and signal quality of soft neural probes, the electronics responsible for wireless signal transmission and their electrical connections still typically use flat and rigid printed circuit boards (PCBs) made from solid, fragile materials (*30*, *31*). These structural and material differences

[1]Department of Materials Science and Engineering, Yonsei University, Seoul 03722, Republic of Korea. [2]Center for Nanomedicine, Institute for Basic Science (IBS), Seoul 03722, Republic of Korea. [3]Department of Energy and Chemical Engineering, Ulsan National Institute of Science and Technology (UNIST), Ulsan 44919, Republic of Korea. [4]Ulsan Advanced Energy Technology R&D Center, Korea Institute of Energy Research (KIER), Ulsan 44776, Republic of Korea. [5]Department of Chemical and Biomolecular Engineering, Yonsei University, Seoul 03772, Republic of Korea. [6]Department of Neurosurgery, Yonsei University College of Medicine, Seoul 03722, Republic of Korea. [7]Department of Neurosurgery, Korea University Anam Hospital, Seoul 02841, Republic of Korea. [8]Graduate Program of Nano Biomedical Engineering (NanoBME), Advanced Science Institute, Yonsei University, Seoul 03722, Republic of Korea.
*Corresponding author. Email: jang-ung@yonsei.ac.kr (J.-U.P.); syleek@yonsei.ac.kr (S.-Y.L.)
†These authors contributed equally to this work.

can compromise the compatibility of the neural interface system with biological systems and hinder its long-term usability in subjects who need to move freely. In contrast to traditional flat and rigid PCBs, the incorporation of stretchable electronic devices offers notable advantages as they can be seamlessly conformed to the curved contours of the body. Moreover, diversifying the structural design is crucial for creating device components with various geometries tailored to individual subjects. For instance, the shape and size of the brain and skull can vary substantially among individuals, and the placement of multiple neural probes must be customized to analyze and stimulate specific brain regions. In this regard, printing techniques borrowed from graphic arts, especially those using direct writing methods, prove valuable for their flexibility in designing various structural configurations. These designs can be quickly adapted using software-controlled printing systems. Therefore, the direct printing of batteries and auxiliary electronics integrated with soft neural probes on the skull can be the key to personalized and customizable neural recording systems.

Here, we report an unconventional direct printing method of a power-integrated, wireless neural recording system that can be formed conformally on the cranium. This printed neural interface system is composed of a quasi–solid-state Zn-ion microbattery (ZIMB), liquid metal–based soft neural probes, and cranial interconnections. Compared to conventional wireless neural interfacing devices, our approach offers several distinct advantages. First, instead of rigid and flat battery shapes, our system seamlessly integrates the electrical power source into the biological system. We achieve this by printing a conformal quasi–solid-state ZIMB on the nonplanar cranial surface to simultaneously meet geometrical and energy requirements. In addition, this printing method, which allows stacking of multilayered electrodes, offers an increase in the areal capacity within a confined area of the cranium, thus enhancing the operation time of this neural recording device. To address battery-related safety risks, we use an aqueous quasi–solid-state electrolyte, which is nonflammable and leakage-free, compared to conventional liquid-state organic electrolytes (*32*). Second, we form soft neural probes with fine dimensions resembling single neurons through high-resolution printing of a liquid metal, eutectic gallium-indium alloy (EGaIn; 75.5% gallium and 24.5% indium by weight). These neuron-like dimensions of soft liquid metal neural probes minimize inflammation and immune responses by ensuring mechanical compatibility with the brain. The probe structures can be precisely controlled by printing conditions, allowing adaptation to various depths and locations within the brain. In addition, the self-healing properties of liquid metal provide stable electrical conduction, even under potential stresses or undesired deformation. Third, cranial interconnections are directly printed along the cranium in vivo to electrically connect soft neural probes implanted in multiple brain regions. This monolithically integrated system (i.e., the liquid metal for all neural probes and interconnects) on the cranium effectively accommodates individual variations in the shape and size of cranium and brain, allowing personalized and customizable configurations for individual's specific needs. Our approach involves a stepwise process, beginning with (i) printing and inserting neural probes in the brain, (ii) printing interconnections on the cranium, and (iii) printing ZIMB. This printed bioelectronics can offer reliable wireless neural recording of multiple brain regions with bio-conformable, customizable configurations within the confined cranium area. Furthermore, our in vivo integration presents good stability in mice through open field tests, heat generation tests, and biocompatibility assessment. We also demonstrate stable wireless neural recording of local field potentials (LFPs), single-unit traces, and principal components analysis (PCA)–clustered single-unit spikes from 16 different brain regions in freely moving mice.

RESULTS

Nonplanar 3D printing of quasi–solid-state ZIMBs for cranium electronics

As a prerequisite to implementing the power-integrated cranium electronics, the ZIMB needs to be geometrically synchronized with the cranium surface. For this purpose, the ZIMB was 3D-printed directly on the nonplanar surface of an implantable cranium model, as schematically illustrated in Fig. 1A. Here, the micro–computed tomography (micro-CT) scanning of a living mouse head yielded a skull image of its 3D geometry, which then allowed the fabrication of an implantable cranium model using a commercial additive manufacturing method. Then, functional inks for each battery components (i.e., cathode, anode, electrolyte, and packaging substance) were successively deposited conformally onto this cranium surface using a direct ink writing (DIW)–based nonplanar 3D printing (fig. S1). The resulting conformal ZIMB was composed of a gold (Au) current collector, manganese oxide (α-MnO_2) powder–based cathode, Zn powder–based anode, and ultraviolet (UV)–cured aqueous quasi–solid-state gel composite electrolyte, together with a UV-cured resin packaging (Fig. 1A). Previous approaches to directly fabricating or transferring power sources on biological tissues have often suffered from dimensional and physical mismatches between flat, rigid electronic batteries and nonplanar, soft tissue surfaces (*33*–*35*). However, in contrast, our 3D printing of battery component inks on the nonplanar cranium model surface conformably formed the ZIMB with its seamless interface between the cranium and battery. This ZIMB-preprinted cranium model can be directly implanted into the skull of a living animal for wireless neural recording in subsequent processes.

The electrode inks consisted of the active materials (i.e., α-MnO_2 and Zn powders), single-walled carbon nanotube (SWCNT) conductive additives, and cellulose nanofiber (CNF)/tetramethylpiperidin-1-oxyl radical–oxidized CNF (TOCN) binders dispersed in an ethylene glycol solvent. The CNF/TOCN binder played a viable role in tuning the dispersion state and rheological properties of the electrode inks. The CNFs are known to form intermolecular hydrogen bonding because of their hydroxyl functional groups (fig. S2, top) (*36*), thus affecting rheological properties of the electrode inks. Meanwhile, the TOCNs in the SWCNT/TOCN suspension could wrap the SWCNTs conformally via intermolecular, noncovalent hydrophobic attraction (*37*–*39*). The Raman spectra of the SWCNT/TOCN [= 2/1 (w/w)] suspension (fig. S3) showed an upshift in the D-band (from 1343 to 1355 cm^{-1}) and in the G-band (from 1580 to 1593 cm^{-1}) positions compared to those of the pristine SWCNT, verifying the intermolecular interaction between the SWCNTs and the TOCNs. The resulting TOCN-wrapped SWCNTs exhibited interparticle electrostatic repulsion enabled by the anionic carboxyl groups of the TOCN (fig. S2, bottom).

To investigate an advantageous effect of the TOCN binder on the dispersion state of electrode inks, a cathode ink (solid content = 0.1 wt %, CNF/TOCN binder dissolved in ethylene glycol) was prepared and compared with a control cathode ink [polyvinylidene

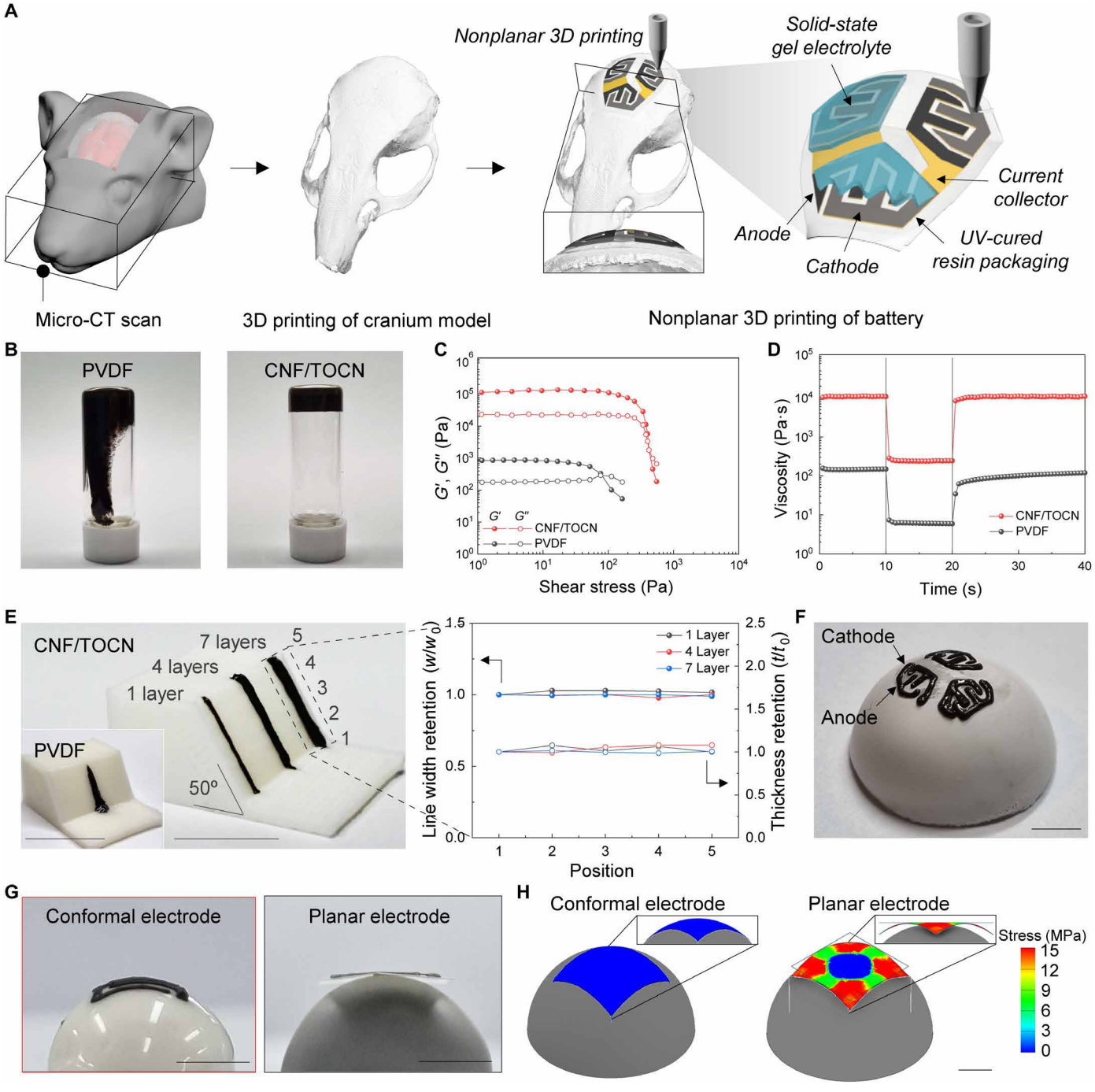

Fig. 1. Nonplanar 3D printing of ZIMBs for cranium electronics. (**A**) Schematic illustration depicting the nonplanar 3D printing of the ZIMB and its components on nonplanar surfaces. (**B**) Photographs of the CNF/TOCN binder (versus PVDF binder)–based cathode inks (solid content, 20 wt %). (**C**) Viscoelastic properties (G' and G'') of the CNF/TOCN binder (versus PVDF binder)–based cathode inks as a function of shear stress. (**D**) 3ITT profiles of the CNF/TOCN binder (versus PVDF binder)–based cathode inks after inducing structural disruption by increasing shear rate (from 0.05 to 1 s^{-1}). (**E**) Linewidth retention (w/w_0) and thickness retention (t/t_0) of the layer-by-layer 3D-printed cathode inks at different positions of the ramp-shaped substrate (slope of 50°) as a function of printed layers. The inset image shows the PVDF binder–based fluidic cathode ink on the ramp-shaped substrate. Scale bars, 20 mm. (**F**) Photograph of the nonplanar, 3D-printed, thick cathodes and anodes on a hemisphere-shaped curvilinear substrate (curvature radius, 10 mm). Scale bar, 5 mm. (**G**) 3D-printed conformal electrode (left) and control planar electrode printed on a PET film (right) integrated with hemisphere-shaped curvilinear substrates (curvature radius, 3 mm). Scale bars, 2 mm. (**H**) FEA of the 3D-printed conformal electrode (left) and control planar electrode printed on a PET film (right) integrated with hemisphere-shaped curvilinear substrates (curvature radius, 3 mm). Scale bar, 2 mm.

fluoride (PVDF), an extensively used binder for ZIB cathodes] dissolved in *N*-methyl-2-pyrrolidone (NMP) as a supplementary experiment. The dispersion state of the CNF/TOCN-based cathode ink remained almost unchanged after being stored for 4 weeks, whereas severe sedimentation was observed in the control PVDF-based cathode ink (fig. S4). This result was confirmed by measuring the zeta potential values of the inks. The CNF/TOCN-based ink showed a more negative zeta potential value of −39.6 mV compared to −10.4 mV of the control PVDF-based ink (fig. S5). A zeta potential value above ±30 mV is known to reflect a stable dispersion state enabled by interparticle electrostatic repulsion (*40*, *41*).

Regulating the viscoelasticity of inks is crucial in ensuring reliable 3D printing on arbitrary curvilinear surfaces (*42*, *43*). The rheological properties of the battery component inks were controlled on the basis of the Derjaguin-Landau-Verwey-Overbeek theory (*44*), with a focus on interparticle attractive and repulsive interactions. The cathode ink (which had a solid content of 20 wt %) with the CNF/TOCN binder showed a higher viscosity and strong shear-thinning behavior compared to the control ink with the PVDF binder (Fig. 1B and fig. S6). Moreover, the cathode ink with the CNF/TOCN binder exhibited a crossover of the elastic (G') and loss (G'') moduli, which represents a thixotropic behavior (*45*, *46*), at a higher yield stress (420 Pa) compared to that of the control ink with the PVDF binder (96 Pa) (Fig. 1C). This result indicates the enhanced structural stability of the cathode ink against gravitational deformation during nonplanar 3D printing. Three-interval thixotropy tests (3ITTs) of the cathode ink, which monitor the change in the viscosity by increasing the shear rate, were conducted to examine the structural recovery of the ink that can affect their shape retention after 3D printing. The cathode ink with the CNF/TOCN binder showed immediate viscosity recovery (~100%) compared to that (~80%) of the control ink with the PVDF binder (Fig. 1D), indicating strong interparticle interactions. In addition, the Zn anode ink with the CNF/TOCN binder showed typical shear thinning (fig. S7A), thixotropic viscoelasticity (fig. S7B), and immediate viscosity recovery (fig. S7C) compared to the control anode ink with the PVDF binder.

On the basis of this understanding of the rheological behavior of the electrode inks, their 3D printability on nonplanar surfaces was investigated. The cathode ink was printed on a 3D-ramp substrate with a steep slope (50°) (movie S1). The linewidth retention (w/w_0) and thickness retention (t/t_0) of the layer-by-layer 3D-printed cathodes exhibited uniform patterns without structural disruption and lateral spreading at different positions of the ramp substrate (Fig. 1E and figs. S8 and S9). By comparison, the PVDF-based cathode ink spread immediately upon deposition. Furthermore, 3D-printed thick cathodes with an interdigitated configuration were fabricated successfully on a flat substrate (figs. S10 and S11) and even on a hemisphere-shaped curvilinear substrate with its curvature radius of 10 mm (Fig. 1F). The dimensional stability of these 3D-printed thick electrodes with the CNF/TOCN binder was confirmed by analyzing their cross-sectional structure. The CNF/TOCN binder and SWCNT conductive additive were dispersed uniformly in the electrodes (figs. S12 and S13). Their nanofibrous structure allowed the structural stability through their physical intermingling with electrode active materials, thereby constructing the thick (even 240 μm for seven layers) and high–aspect ratio electrodes (fig. S14). We noted that the thick cathodes beneficially contributed to the higher areal capacity of the ZIMB.

In addition to these structural benefits, the hydrophilic CNF/TOCNs and the highly electrically conductive SWCNTs serve as channels for electrolyte access and electron transport, respectively, which is more pronounced in the thick and high–mass loading electrodes. It is known that electrodes with high mass loading are prone to sluggish redox kinetics due to the elongated electrical and ionic pathways in their structure, resulting in unwanted capacity degradation (*47*). The contact angle measurements of an aqueous electrolyte (2 M $ZnSO_4$/0.2 M $MnSO_4$) on both CNF/TOCN- and PVDF-based cathodes were performed. A lower contact angle was observed for the CNF/TOCN-based cathode (35.5°) compared to the PVDF-based counterpart (136.5°), indicating a higher affinity toward the aqueous electrolyte (fig. S15). In addition, the CNF/TOCN-based MnO_2 cathode exhibited higher electrical conductivity (18.4 S cm^{-1}) in contrast to the PVDF-based cathode (0.11 S cm^{-1}) (fig. S16), underscoring the advantageous role of the homogeneously distributed SWCNT electronic networks.

The shape conformability of these electrodes was investigated further by observing their integration onto the hemisphere-shaped curvilinear substrates with various curvature radii (fig. S17). Control samples were fabricated by printing the identical electrode materials and dimensions on a planar polyethylene terephthalate (PET) film followed by pressing onto curvilinear substrates. The contact area ratio (defined as the ratio of contact area between the printed electrode and underlying substrate to the total area of the printed electrode) was evaluated (fig. S18). The nonplanar 3D-printed electrodes on the curvilinear substrates exhibited thorough contact (reaching a contact area ratio of ~100%) even at smaller curvature radius (3 mm), whereas the control electrodes showed large and irregular gaps with the underlying substrates (Fig. 1G). This superior conformability of the 3D-printed electrodes was verified by quantitatively identifying the low deformation stress and uniform distribution using finite element analysis (FEA) (Fig. 1H). These results demonstrated that the CNF/TOCN-based electrode inks, combined with the nonplanar 3D printing, enabled the geometrical matching with the arbitrarily shaped curvilinear substrates.

In addition to the electrodes described above, other battery components, including separator membranes, electrolytes, and packaging substances, should be integrated conformally with the complex-shaped cranium. A 3D-printed quasi–solid-state gel composite electrolyte ink was composed of an aqueous electrolyte (2 M $ZnSO_4$ + 0.2 M $MnSO_4$), UV-curable acrylamide monomers as a mechanical skeleton, and SiO_2 nanoparticles (average particle size ~40 nm) as a rheology-tuning agent (fig. S19). The printed gel composite electrolyte was solidified after exposure to UV irradiation, which enabled it to serve as both the separator and ionic medium (ionic conductivity: 6.1×10^{-3}) between the cathode and anode of the ZIMB. The UV cross-linking of acrylamide was verified by observing the change in characteristic Fourier transform infrared (FTIR) peaks assigned to acrylic C═C bonds (1620 to 1640 cm^{-1}) (fig. S20). The packaging ink consisted of a commercial UV-curable resin (*48*, *49*) and SiO_2 nanoparticles. The gel composite electrolyte and packaging ink showed well-tuned viscoelastic properties suitable for 3D printing (fig. S21) (*50*).

Cranium-customized ZIMBs and their electrochemical characteristics

The battery component inks prepared above were printed sequentially on top of the 3D cranium model to fabricate a quasi–solid-state ZIMB with its structure synchronized to fit the geometrical shape of this cranium model (Fig. 2A, fig. S22, and movie S2). This ZIMB consisted of three-unit cells connected in series (reaching a

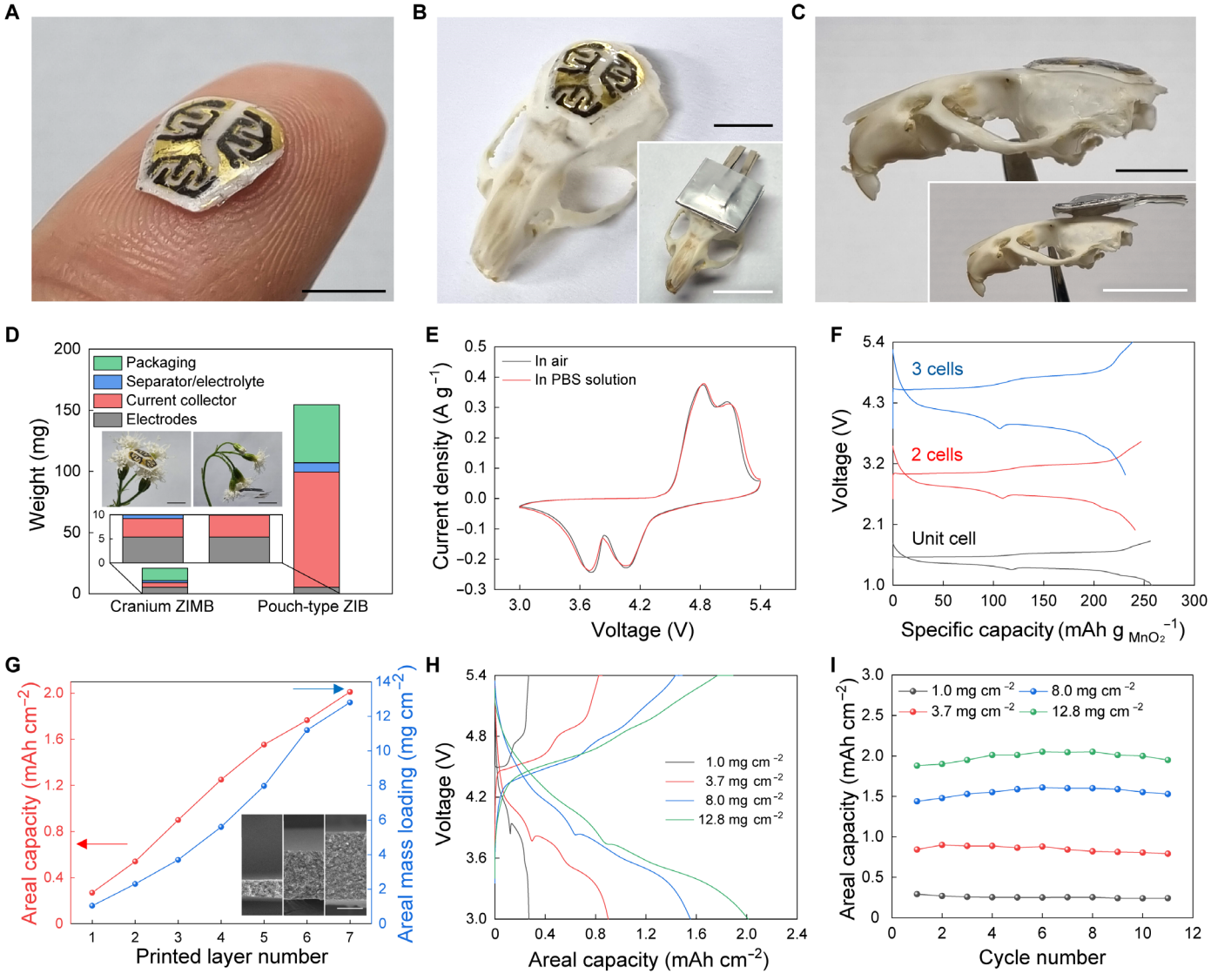

Fig. 2. Cranium-customized ZIMBs and their electrochemical characteristics. (**A**) Photograph of the cranium-customized ZIMB fabricated via DIW-based nonplanar 3D printing. Scale bar, 5 mm. (**B**) Photographs (top view) of the cranium-customized ZIMB and control pouch-type ZIMB (inset) integrated with a real mouse cranium. Black scale bar, 5 mm. White scale bar, 10 mm. (**C**) Photographs (side view) of the cranium-customized ZIMB and control pouch-type ZIMB (inset) integrated with a real mouse cranium. Black scale bar, 5 mm. White scale bar, 10 mm. (**D**) Comparison of the weight between the cranium-customized ZIMB and control pouch-type ZIMB in terms of battery components. The inset (bottom) shows the magnified graph of the weight of electrodes. The insets (top) show photographs verifying the weight difference of the cranium-customized ZIMB and control pouch-type ZIMB. Scale bar, 5 mm. (**E**) CV curves of the cranium-customized ZIMBs in air and PBS solution at a scan rate of 0.2 mV s^{-1} and voltage range of 3.0 to 5.4 V. (**F**) Charge/discharge profiles of the cranium-customized ZIMBs at a charge/discharge current density of 0.1 A g^{-1} as a function of cell number. (**G**) Areal capacity of the ZIMB and areal mass loading of cathodes as a function of printed layer number. The insets show the cross-sectional SEM images of the one-, four-, and sever-layer printed cathodes. Scale bar, 100 μm. (**H**) Charge/discharge profiles of the cranium-customized ZIMB as a function of areal mass loading of cathodes for a voltage range of 3.0 to 5.4 V and charge/discharge current density of 0.1 A g^{-1}. (**I**) Cycling performance of the cranium-customized ZIMBs as a function of areal mass loading of cathodes at a charge/discharge current density of 0.1 A g^{-1}.

voltage of 5.4 V) that were needed to power all deep-brain recording probes (fig. S23). Notably, this ZIMB exhibited a minimal dead space, which enabled the maximization of its stored energy in a confined area (smaller than 7.7 mm by 7.9 mm) of the underlying cranium.

This resulting ZIMB was implanted to the cranial surface of a living mouse and exhibited its seamless unitization (Fig. 2, B and C), in contrast to a conventional pouch-type battery with a rectangular shape and rigid components (fig. S24). Considering that the weight of a conventional battery typically comprises more than 20% of the total device weight (*17*, *51*, *52*), reducing the battery weight can be the key to alleviating the physical stress of a living mouse with assisting its naturally moving behaviors for cranium-implantable electronics. In particular, natural behaviors elicit specific cortical spectral power patterns compared to constrained conditions, enhancing our knowledge of neurobehavioral variability (*16*). Figure 2D shows that our printed ZIMB was notably lighter compared to the pouch-type

ZIMB, while there was no appreciable difference in the weight of active materials in the electrode. For example, the weight of the printed ZIMB was substantially reduced by replacing the current collector materials from heavy metal foil to thin Au (thickness: 1 μm). These results highlight the practical viability of our ZIMB as a lightweight power source for wireless deep-brain analysis systems that can be geometrically customized to the shape of a subject's cranium.

The electrochemical properties of our cranium-customized ZIMB were investigated. To explore its practical viability for bioimplantable electronics, this printed battery was immersed in a phosphate-buffered saline (PBS) solution for electrochemical characterization. There was no change in the ZIMB's weight after immersion in PBS solution for 3 weeks (fig. S25). Moreover, the cyclic voltammetry (CV) analysis in the PBS solution revealed the normal characteristic redox voltages assigned to Zn^{2+}/H^{+} insertion and extraction from the MnO_2 cathodes in this solution (Fig. 2E). The charge/discharge profiles of the ZIMB in series configuration were investigated as a function of cell number (Fig. 2F). The cutoff charge voltages of the resulting cells increased from 1.8 V (unit cell) to 5.4 V (three cells) with increasing the cell number while maintaining the specific capacity of the MnO_2 active materials. Notably, the ZIMB with three cells connected in-series showed normal charge/discharge behavior and higher specific capacities at various current rates compared to control cells with the PVDF-based electrodes (fig. S26). This improvement verifies the facilitated redox kinetics (notably, the reliable intercalation/deintercalation of Zn^{2+} ions) of MnO_2 cathode active materials enabled by the intertwined nanofibrous SWCNT and CNF/TOCN networks. The ZIMB also showed long capacity retention (70% after 500 cycles) at a current density of 1.0 A g^{-1} (fig. S27) in an operating voltage range of 3.0 to 5.4 V. The temporary increase in discharge capacity during the initial cycles was attributed to the activation of the MnO_2 active materials, which has been commonly observed in typical Zn-MnO_2 cells (*53*–*55*). The areal capacity of the ZIMB can be adjusted by sequential layer-by-layer printing of the electrodes. We note that higher areal capacity is preferred to enable longer operation time of wireless deep-brain analysis systems. The areal mass loading and corresponding areal capacity of the MnO_2 electrode showed an increase in proportion to the number of printed electrode layers, reaching as high as 12.8 mg cm^{-2} and 2.0 mAh cm^{-2} at the seven-layer printed electrode, respectively (Fig. 2G). With this high areal capacity of the ZIMB, the operation time of a commercial Wi-Fi module reached approximately 2 min without recharging of the ZIMB. Over a wide range of the areal mass loadings (1.0 × 12.8 mg cm^{-2}), the printed electrodes exhibited normal charge/discharge behavior (Fig. 2H) and stable cycling performance (Fig. 2I).

Printing of soft neural probes using liquid metals

For deep-brain analysis, we fabricated liquid metal–based, soft neural probes through a high-resolution printing of liquid metals. Figure 3A illustrates our direct printing system. This system is composed of a nozzle connected to an ink reservoir, a pneumatic pressure controller, and a six-axis stage with programmable movements in the *x*, *y*, or *z* axis and two tilting axes in the *xy* plane (*29*). For the direct printing of liquid metals, we prepared two types of nozzles: (i) glass capillaries with inner diameters ranging from 5 to 60 μm and (ii) commercial syringe needles with metal tips with inner diameters of 100, 120, and 140 μm. Then, a nozzle was mounted onto a syringe-type ink reservoir that contained EGaIn (as an ink), and a substrate was placed on the six-axis stage. For the nozzle with its inner diameter of 5 μm, the distance between the nozzle and the substrate was controlled to be ~2 μm, and a pressure of 55 psi was applied to extract the EGaIn ink through a nozzle. Then, the direct printing of EGaIn was performed by controlling the on/off operation of this pneumatic pressure and the movements of the stage. As example, Fig. 3B shows an optical micrograph and a scanning electron micrograph (SEM) of the printed EGaIn lines (linewidth: 5 μm) with adaptable lengths. These printed patterns imply the fabrication of soft neural probes with various shapes and lengths. Figure 3C presents the linewidth of the EGaIn printing with respect to the inner diameter of the nozzle at a constant printing velocity of 0.1 mm s^{-1}. The linewidth increased almost linearly with the nozzle's inner diameter. For the fabrication of soft neural probes, EGaIn lines of 5 μm in width were printed directly on a parylene-C film (thickness: 1 μm). Afterward, we vacuum-deposited an encapsulation layer of parylene-C with its thickness of 1.5 μm on the printed EGaIn lines and then selectively opened the tip areas of EGaIn electrodes for interfacing neurons. Platinum nanoclusters, denoted as platinum black (PtB), were formed by electrodeposition at the open area of these EGaIn electrodes (Fig. 3, D and E). Figure S28 shows the optical micrograph and the SEM of the fabricated top part of the soft neural probes. The overall fabrication process is schematically illustrated in fig. S29. The deposition of PtB improved the quality of the signal by lowering the impedance of the electrodes, as the PtB nanostructures increased the surface area for electrochemical reaction. Figure 3F shows the impedance spectroscopy of the PtB-coated liquid metal (PtB/EGaIn) and the pristine EGaIn probes (without PtB). The impedances (at 1 kHz) of the PtB/EGaIn probes and the EGaIn probes were 387.5 and 1141.5 kilohms, respectively, presenting three times lower impedance in PtB/EGaIn. Furthermore, the impedance (at 1 kHz) of our probe for 7 days was measured by immersing in PBS solution (75°C for 7 days; a day is equivalent to a month in the normal environment). As plotted in fig. S30, the result exhibited negligible change in impedance, showing long-term stability of our probe. To compare the impedance with other well-known materials used for conventional neural interfacing electrodes, the normalized impedance value with respect to open contact area to neural tissue, denoted as area-specific impedance (ASI), was plotted in Fig. 3G (*56*). According to the results, the ASI of the PtB/EGaIn was 15.2 ohm mm^2, and this value was about one-third that of the pristine platinum. In addition, the ASI of EGaIn, 44.8 ohm mm^2, was comparable to that of platinum, which has been used extensively in neural recording electrodes due to its low impedance with high signal quality.

The softness of the neural probes is one of the main factors that enable long-term recording at the brain tissue–electrode interface since it can prevent inflammation and tissue damage by alleviating mechanical mismatches (*57*). To compare the softness of EGaIn and PtB/EGaIn with other solid metals and conducting polymers that are used in previous neural interfacing electrodes, we measured the elastic modulus of EGaIn and PtB/EGaIn by tensile tests (Fig. 3H). The results indicated that the elastic modulus of PtB/EGaIn was 211 kPa, and this value was about six orders of magnitude lower than that of platinum and was about four orders of magnitude lower than that of poly(3,4-ethylene dioxythiophene) (PEDOT). When we compared the elastic moduli of PtB/EGaIn and EGaIn, there was no notable difference between them due to the nanoscale thickness of the PtB layer. Bending stiffness is another physical quantity related to the rigidity of

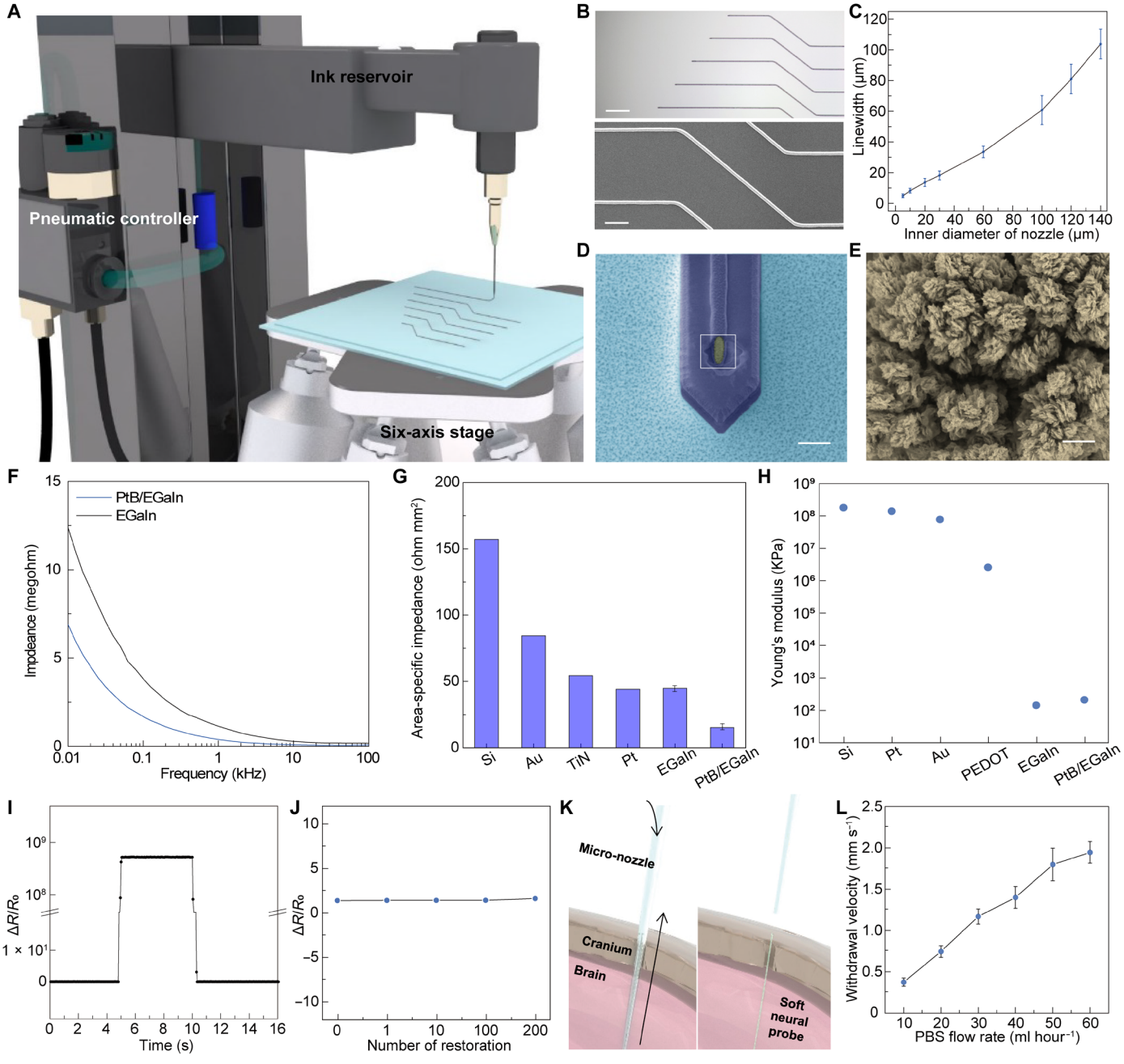

Fig. 3. Printing of soft neural probes using liquid metals. (**A**) Schematic illustration of a printing system of liquid metal. (**B**) Optical micrograph and SEM of printed liquid metal patterns with various shapes and lengths. Scale bars, 200 μm (top) and 50 μm (bottom). (**C**) Plot of linewidths of printed liquid metals according to the inner diameters of the nozzles at a constant printing velocity of 0.1 mm s^{-1}. Each data point indicates the average of five measurements, and the error bars represent the SD. (**D**) Colorized SEM of a fabricated soft neural probe. Dark blue and dark yellow colors correspond to parylene-C and PtB-coated EGaIn, respectively. Scale bar, 10 μm. (**E**) SEM of the magnified view of PtB indicated by the white dotted box in Fig. 3D. Scale bar, 1 μm. (**F**) Impedance spectroscopy of pristine EGaIn- and PtB-coated EGaIn probes. (**G**) Comparison of area-specific impedance of silicon, gold, titanium nitride, platinum, pristine EGaIn, and PtB/EGaIn. The error bars represent the SD of five measurements. (**H**) Comparison of elastic moduli of silicon, platinum, gold, PEDOT, pristine EGaIn, and PtB/EGaIn. (**I**) Real-time change in the resistance of a PtB/EGaIn during disconnection and restoration by pressing and releasing, respectively. (**J**) Relative change in resistance of PtB/EGaIn during disconnection and restoration for 200 times. (**K**) Schematic illustration of the syringe injection method of soft neural probe by balancing the flow rate and nozzle withdrawal velocity using our printing system. (**L**) Relationship between the flow rate of PBS with a probe and withdrawal velocity of nozzles with an inner diameter of 100 μm. Each data point indicates the average of five measurements, and the error bars represent the SD.

the neural probe, and it needs to be considered to determine the degree of mechanical mismatch between the brain tissue and neural probe. By taking advantage of the intrinsic softness and overall thinness of the PtB/EGaIn probe, its effective bending stiffness was 0.264 pN m, which is comparable to that of brain tissue (*58*).

For the long-term neural recording of brain signals from freely moving subjects, stable electrical conduction of neural probes is also essential for their long-term usage, in addition to the softness of the neural probes. The self-healing ability of liquid metals can overcome the problem of unwanted electrical disconnection that can be often observed in conventional solid metal–based neural probes due to microcrack formation under dynamic conditions (*59*). Figure 3I shows the real-time relative change in the electric resistance of PtB/EGaIn. For this test, the PtB/EGaIn electrode was disconnected by pressing it down for 5 s, which increased its resistance notably. After releasing this pressing, the resistance was recovered to similar to its initial state within 5 s at ambient conditions due to the spontaneous and rapid coalescence of EGaIn liquid metal. Here, the parylene-C encapsulation layer, the ultrathin gallium oxide skin (thickness < ~3 nm), and thin Pt nanoclusters of this EGaIn pathway can prevent Ga from spreading, and the interior of the printed electrode remain at the liquid state to allow their large deformability. Thus, applying external compressive pressures to rupture only this ultrathin oxide skin and Pt nanoclusters (without parylene-C) enables EGaIn to flow out and connect with adjacent liquid metal parts, thereby forming conductive paths locally under the pressed area within the parylene-C layer. Then, these coalescent conductive paths of EGaIn inside the parylene-C encapsulation can be maintained reliably because of the good softness and self-healing capability against mechanical deformations without any physical damage of parylene-C layer (fig. S31). In addition, as shown in Fig. 3J, this self-healing ability to restore electrical conduction was further tested in wet conditions to mimic the environment of the implanted neural probes surrounded by cerebrospinal fluid in the brain. The electrical disconnection and reconnection of PtB/EGaIn were repeated 200 times in a PBS solution. The electrical restoration of PtB/EGaIn was consistent in PBS solution to show its good self-healing ability.

While the good softness (comparable to the brain case) and self-healing ability of our neural probes provide the advantages stated above, their delivery to specific brain regions is not compatible with the conventional direct insertion method that uses rigid solid-state neural probes (with higher bending stiffness than brain tissue) (*6*, *18*, *20*–*22*). To target different regions of the brain precisely without crumpling and buckling problems during the probe injection, we used direct syringe injection through a glass capillary nozzle (*10*). First, a soft neural probe suspended in a PBS solution was drawn and loaded into a glass capillary. Then, the probe and capillary were implanted into specific brain regions with a slow insertion rate of 0.02 mm s^{-1} to minimize the potential damage to the tissue during this injection (*60*). A syringe pump connected to the nozzle and our printing system with a microscope camera (QImaging Micropublisher 5.0 RTV, Teledyne Photometrics) were used to inject the probe by balancing the PBS flow rate and the velocity at which the nozzle was withdrawn (Fig. 3K). Figure 3L shows the relationship between the flow rate of the PBS and the withdrawal velocity of the nozzle with inner diameter of 100 μm. The PBS flow rate increased almost linearly with the withdrawal velocity of the nozzle, and smooth injection was achieved for PBS flow rates in the range of 10 to 60 ml $hour^{-1}$. With this injection method, we controlled the exposed range of the outer end of our PtB/EGaIn neural probe precisely on the predrilled hole of the cranium. Similarly, multiple probes could be sequentially inserted into different brain regions.

In vivo integration of a power-integrated wireless neural recording system on the cranium

In vivo integration of our wireless neural recording system with the conformal quasi–solid-state ZIMB was formed along the cranium curvature of a living mouse. Here, the direct printing of EGaIn interconnections on the cranium enabled the integration of all device components, including implanted neural probes, a commercial Wi-Fi unit (JAGA Penny, Jinga-hi, USA, size: 1 × 3 cm), and ZIMB, as a cranium electronic system. Figure 4A illustrates the entire layout of our printable power-integrated neural recording system that was formed on the cranium where a medical-grade polymeric insulating layer was preprinted. The overall procedure of this integration is schematically illustrated in fig. S32. First, a mouse (C57BL/6N, 12 weeks) was anesthetized intraperitoneally with a mixture of 20 μl of xylazine, 80 μl of ketamine, and 100 μl of PBS. Then, the mouse was fixed on the rodent adaptor composed of ear bars and jaw cuff (RWD Life Science, USA) to minimize the vibration from heartbeat and breathing. Second, a transparent passivation layer of medical-grade polymer (Loctite 4011, Henkel, Germany) was printed on the cranium surface to prevent the interference between signals and electrical leakage through the wet cranium and to ensure the safety of the circuit with respect to the cranial bone tissue. Third, our soft neural probes were implanted stereotaxically in predrilled holes in the cranium using the syringe injection method, and EGaIn interconnections were printed along the cranial surface to form the electrical connection with the implanted neural probes (fig. S33). For example, Fig. 4B shows the integration of a total of 16 implanted probes with a Wi-Fi communication chip by directly printing EGaIn interconnections on the cranium of a living mouse with the minimum linewidth of 5 μm. During this printing, the distance between the tip of the nozzle and the cranial surface was maintained to be 5 μm by controlling the *z* axis of printing stage, and the constant pneumatic pressure of 55 psi was applied (movie S3). Fourth, after covering the entire printed circuitry using a medical-grade silicone elastomeric adhesive (Kwik-Sil, World Precision Instruments, USA), this wireless neural recording circuitry was subsequently integrated with the preprinted ZIMB component (Fig. 4C). This ZIMB could act as a power source that fits conformally to the cranium surface with high areal capacity, thereby enabling continuous operation of our wireless neural recording device in a miniaturized size that could be placed within the confined space of the mouse's cranium. Last, an encapsulation layer of antibiotic-loaded bone cement (Cemex RX, TECRES) was deposited to the entire surface for the seamless fixation of our electronic system to the cranium, followed by the suturing of the scalp. A block diagram of this entire system is shown in fig. S34.

The printing of this integrated system on the cranium eliminated the necessity of bulky configurations of batteries, allowing free and natural movement of subjects. Figure 4D shows the representative trajectories of the normal mouse and the cranium system–implanted mouse during their open field test. Before this test, mice were housed at 23°C temperature and 50% humidity, with a 12-hour light/12-hour dark cycle for 7 days. Each mouse activity was recorded for 5 min in an open field arena (movie S4). Then, we analyzed their travel distance and duration spent in the center zone using an ANY-maze software (version 4.3; Stoelting Co., Wood Dale, IL). (The

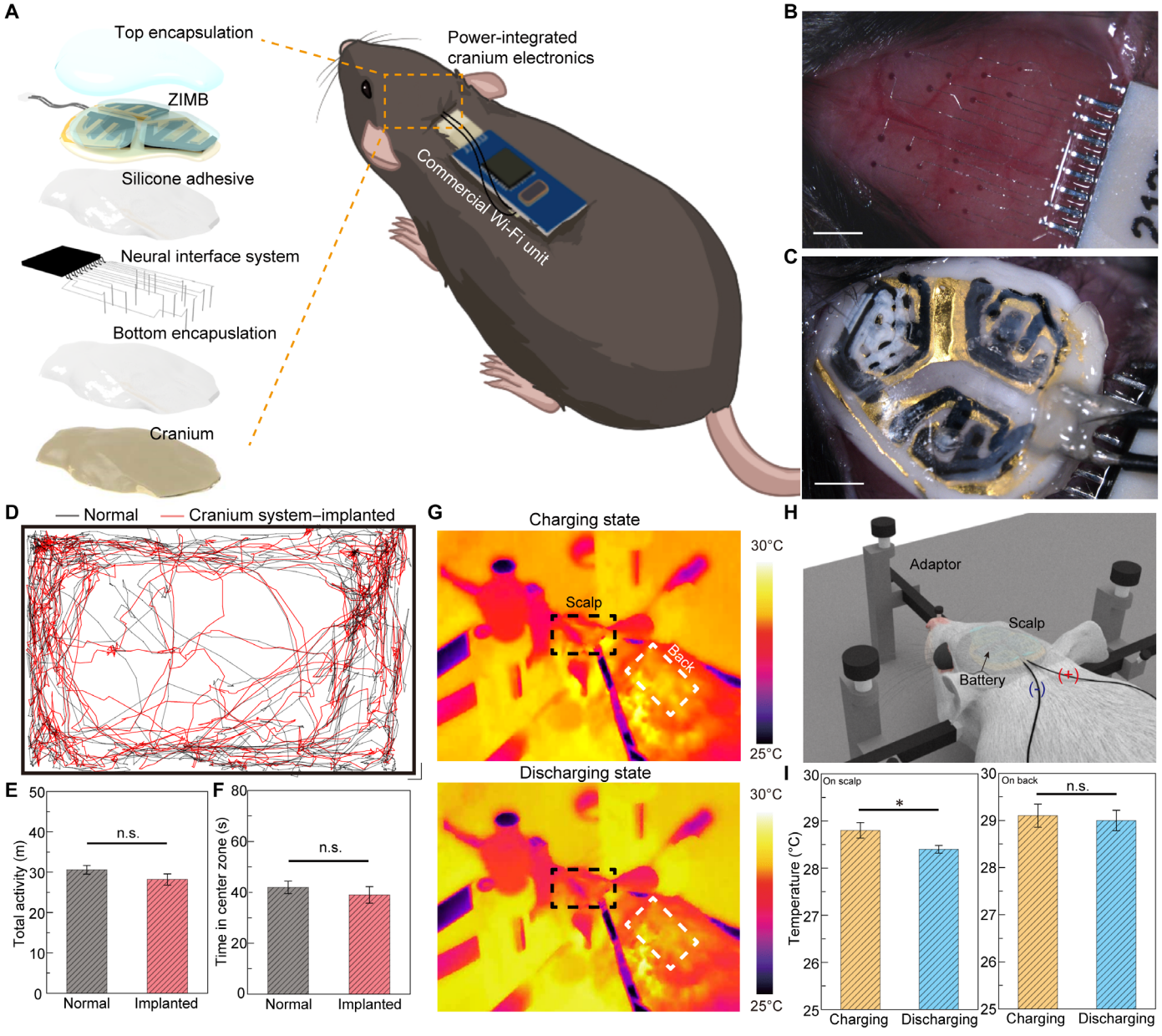

Fig. 4. In vivo integration of a power-integrated wireless neural recording system on the cranium. (**A**) Schematic illustration of the entire layouts of a printable power-integrated wireless neural recording system on the cranium. (**B** and **C**) Optical stereomicrograph of liquid metal–based neural interface applied to a mouse cranium (B) and ZIMB integration on the neural interface (C). Scale bars, 1 mm. (**D**) Representative trajectories of normal mice and the cranium system–implanted mice in an open field arena for 5 min. Scale bars, 3 cm (vertical) and 3 cm (horizontal). (**E**) Comparison of overall distance between normal mice ($n = 3$) and cranium system–implanted mice ($n = 3$). The error bars represent the SD. Statistical analyses were performed by the two-tailed unpaired t test, $P = 0.4474$ (n.s., not significant). (**F**) Comparison of time spent in the center zone between normal mice ($n = 3$) and cranium system–implanted ($n = 3$). The error bars represent the SD. Statistical analyses were performed by the two-tailed unpaired t test, $P = 0.4226$. (**G**) IR images of cranium system–implanted mouse during the charging and discharging of ZIMB. (**H**) Schematic illustration of the heat test setup. (**I**) Temperature differences of the scalp (left) and back (right) of the cranium system–implanted mice during the charge and discharge states. The error bars represent the SD with $n = 3$ mice. Statistical analyses were performed by the two-tailed paired t test, $P = 0.0418$ (left) and $P = 0.166$ (right). *$P < 0.05$ was considered significant.

open field arena and its center zone are illustrated in fig. S35.) Their travel distance during the same duration was quantitatively compared as a criterion of natural behaviors in Fig. 4E, and the results showed a negligible difference between that of the control (i.e., normal) and the experimental groups (i.e., the cranium system–implanted). In addition, the time spent in the center zone was measured as a criterion of anxiety-related behavior, with a longer time implying a lower level of anxiety (*61*). As shown in Fig. 4F, the time spent in the center zone by the cranium system–implanted mice was not notably different from the normal mice case, being only 4 s shorter on average during the 5-min test. These results indicated that our cranium electronic system (where all printed forms of a battery, neural probes,

and interconnections were integrated with the Wi-Fi circuitry) did not degrade the natural behavior of the mice.

Conventional power sources, such as Li-ion batteries, usually incorporate flammable liquid organic electrolytes, thereby presenting a substantial risk to wearable and biomedical applications (*62*). In contrast, the implementation of our printable power-integrated cranium electronics revealed no noticeable adverse effects and no abrupt heat generation due to the aqueous quasi–solid-state electrolytes of our ZIMB. The temperature of the scalp and back of the mouse implanted with our cranium electronic system was measured during charging and discharging the ZIMB, as shown in Fig. 4G. The galvanostatic charge/discharge measurements of the ZIMB were performed using a potentiostat/galvanostat (VMP-300, Bio-Logic), and the heat generation of our cranium electronic system implanted to the anesthetized mouse was monitored using an infrared (IR) camera (T650sc, FLIR Systems), as shown in Fig. 4H and movie S5. While charging and discharging of our system, the temperature of the mouse scalp was maintained at the average of 28.8° and 28.4°C, respectively. In addition, the temperature on the back of the mouse was also maintained at the average of 29.1° and 29.0°C in charging and discharging states, respectively (Fig. 4I). The scalp temperature of normal mice under anesthesia is typically measured to be approximately 1°C lower than their back temperature in IR imaging (*63*, *64*). Therefore, considering the average body temperature of the anesthetized mouse (29.2°C), there was no notable heat generation during the operation of our ZIMB-integrated system, indicating its notable potential for use in bioelectronics applications.

Wireless neural recording

To demonstrate the ability to integrate complex configurations of neural probes within a single electronic system, we implanted multiple neural probes across extensive brain regions, and all probes were subsequently integrated into our power-integrated wireless neural recording system using printing EGaIn interconnects directly on the cranium of a living mouse. The intricate and extensive placement of multiple neural probes is essential for the cross-regional study of multiple brain regions to uncover the dynamic neural networks and expanded mapping capability related to behavior experiments. Figure 5A illustrates a configuration of our liquid metal neural probes and EGaIn interconnections before their integration to the ZIMB part. A total of 16 neural probes were implanted in both hemispheres of the brain of a mouse (indicated by black dots), targeting the motor cortices (MO) and hippocampal regions (HIP). The soft neural probes exhibited low impedances of 421.4 kilohms on average with an SD of 11.2 kilohms at 1 kHz, and the open area of each probe electrode was 39.25 μm^2 (Fig. 5B). The 4×4 array in Fig. 5B schematically corresponds to the probe position in Fig. 5A. After integrating each probe to the Wi-Fi communication unit and ZIMB via the printing of EGaIn interconnections on the cranium, we acquired single-unit traces wirelessly at a sampling rate of 20,360 Hz. Single-unit potentials were recorded from eight regions, respectively, in motor cortices and hippocampal regions (Fig. 5C). Movie S6 shows this wireless recording in a freely moving mouse. On the basis of the obtained signals, mean waveforms of PCA-clustered single-unit spikes were plotted in Fig. 5D. Their structurally and mechanically neuron-like properties provided high spatiotemporal resolution for single neuron–scale recordings, detecting one to three mean waveforms of single-unit spikes. In MO 3 channel, three different mean spike waveforms were PCA-clustered with the L ratio of 0.03658, 0.03359, and 0.04332, which indicated a good separation between single-unit spikes (Fig. 5E).

We observed simultaneous activation of multiple brain regions, including the motor cortex and hippocampus, during the posture maintenance in the open field test. Figure 5F shows the LFPs recorded from adjacent MO 1 and MO 2 channels (top), the superimposed beta waves (10- to 45-Hz oscillation) (middle), and their phase angles (bottom) using our cranium electronics system. The superimposed beta waves of the LFPs exhibited similar rhythms and a temporal delay (3.11 ms on average), representing the propagation of oscillations from MO 1 to MO 2 regions. In addition, to verify whether the locomotion of the mouse induces noise in the LFP signal, we quantitatively compared the mean SD of all the baseline amplitudes of beta-filtered LFP signals measured from the motor cortex in moving and resting states of the same mouse (fig. S36) (*65*). The result showed a negligible difference between the moving and resting states, indicating that the locomotion of the mouse induced no notable noise in the LFP signals. Figure 5G shows our recording of the LFPs from the hippocampal region (HIP 6) during the static state before the onset of movement (top), the normalized power spectrogram (baseline-corrected by mean power at each frequency) in the theta frequency (middle), and the average power spectrum (bottom). These results showed the notable increase in theta power during stationary periods, which is consistent with previous findings that theta oscillations in the 6- to 10-Hz range typically dominate the hippocampal LFPs in mice and the theta power increases during the stationary but movement-planning state (*66*).

To test the biocompatibility of our probe, we first evaluated the cytotoxicity of the printed pristine EGaIn. Neuro2a cells, a neuroblast cell type, were used for the evaluation, and cell viability was assessed using the Live/Dead Imaging kit [LIVE/DEAD Cell Imaging Kit (488/570), Thermo Fisher Scientific] after 7 days of culture. The result showed that the sample with printed EGaIn lines exhibited high cell viability, comparable to the control sample, indicating the negligible toxicity of pristine EGaIn (fig. S37). Furthermore, the chronic tissue responses to our neural probes in the MO 3 region were examined 4 weeks after implantation by immunostaining of anti-FOX3 (neuron), anti–Iba-1 (microglia), and anti–glial fibrillary acidic protein (GFAP; astrocyte). Microglia and astrocyte were used as indicators of normal glial responses. Figure S38 shows a cross-sectional confocal micrograph near the implanted probe, and the interface between the probe and brain tissue showed only marginal immune reactions with neither notable depletion of neurons nor the enhancement of microglia and astrocyte. In addition, we conducted histological evaluation of tissue directly contacting our implanted system for further long-term biocompatibility validation. After 6 weeks of implantation, we characterized the scalp of a mouse implanted with our cranium system using hematoxylin and eosin staining. The resulting histology image showed no notable signs of malignancies or inflammation in the scalp in direct contact with our cranium system (fig. S39). The excellent biocompatibility exhibited in these results contributes to the long-term stable operation of our system. To further assess this experimentally, we recorded single-unit potentials and two different PCA-clustered single-unit spikes from a mouse implanted with our cranium system after 6 weeks (fig. S40).

DISCUSSION

We have developed a printable, power-integrated electronic system for wireless neural recording that can be conformally integrated into the

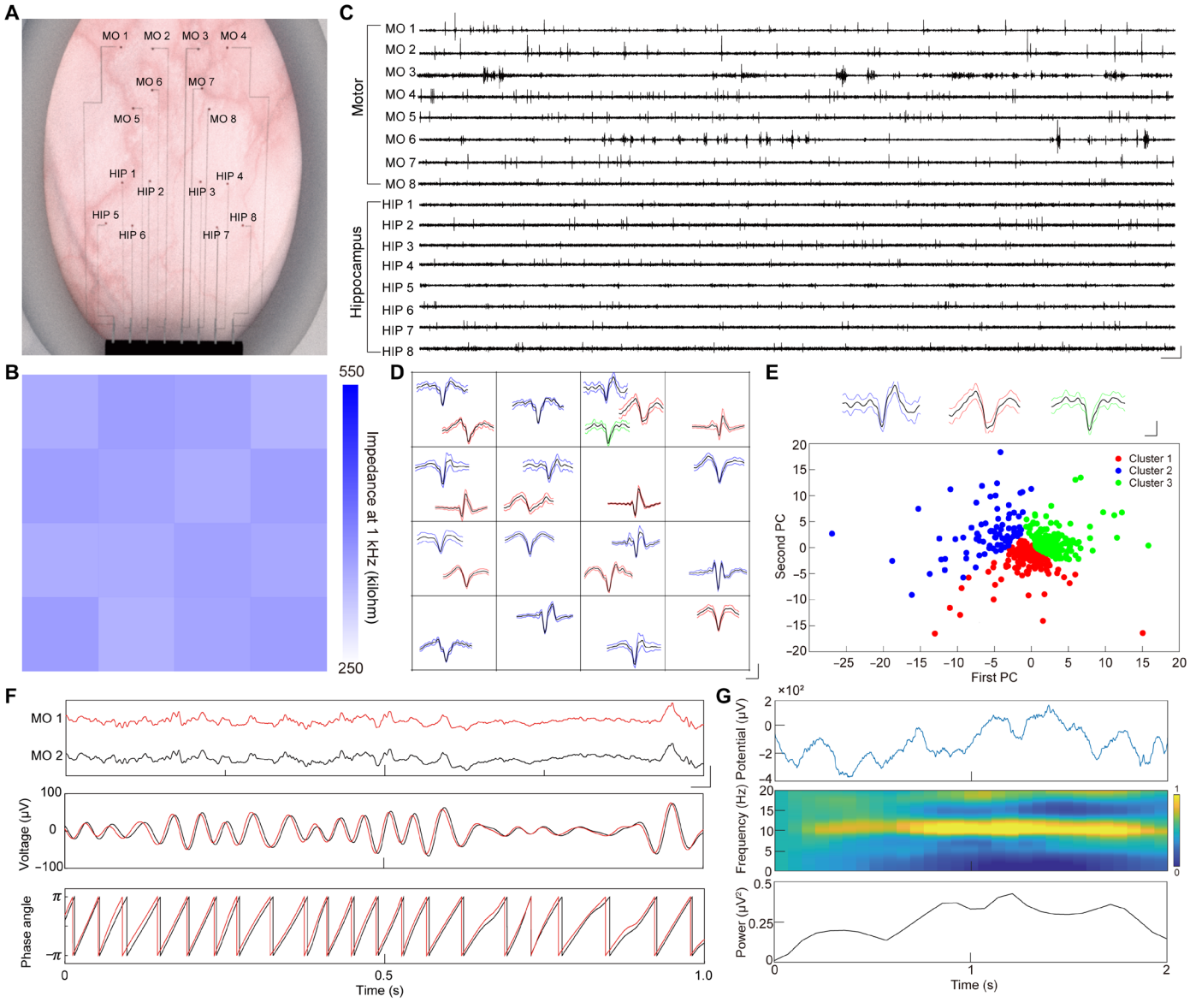

Fig. 5. Wireless neural recording. (**A**) Schematic illustrations showing the relative positions of neural probes and cranial interconnections. (**B**) Impedance mapping of implanted electrode arrays. (**C**) Representative single-unit potentials of 16 different regions of the mouse brain. MO, motor cortex; HIP, hippocampus. Scale bars, 100 μV (vertical) and 200 ms (horizontal). (**D**) PCA-clustered single-unit spikes of 16 different regions of the mouse's brain. Scale bars, 100 μV (vertical) and 2 ms (horizontal). (**E**) Three different PCA-clustered single-unit spikes recorded in MO 3 region. Scale bars, 100 μV (vertical) and 2 ms (horizontal). (**F**) Simultaneous LFPs recorded from two adjacent motor cortices (MO 1 and MO 2 regions). Scale bars, 100 μV (vertical) and 50 ms (horizontal) (top), superimposed beta waves (10 to 45 Hz) (middle), and corresponding phase angles (bottom). (**G**) LFPs recorded from hippocampal region (HIP 6) (top), the normalized power spectrogram (middle), and the average power spectrum (bottom).

cranium of a living subject, maximizing the integrity of electronics to the biological body. For a power source, a quasi–solid-state ZIMB was 3D-printed directly on the nonplanar surface of a cranium model. The seamless interface of ZIMB to the cranium achieved the high areal capacity and ultralight weight of this battery, alleviating physical stress in living mice and assisting their natural behaviors. In addition, soft neural probes were fabricated using high-resolution printing of a low-modulus and biocompatible liquid metal, with cell-scale diameters and adaptable lengths to match various target depths and locations in the brain while achieving minimal invasiveness. The additional formation of platinum nanostructures on the liquid metal surface lowered the electrode's impedance to increase signal quality and spatiotemporal resolution for neural recording. Furthermore, direct printing of liquid metal interconnections along the curved surface of the cranium formed a monolithic integration with these neural probes, which enabled the entire integration of the ZIMB, Wi-Fi communication unit, and multiple neural probes as a power-integrated wireless neural recording system on the cranium. All device components were placed under the skin by subsequent skin closure and suture steps. The in vivo demonstration validated the reliability of our neural recording system within the body and its ability to record LFPs and single-unit spikes from multiple brain regions wirelessly.

Recently, wireless neural recording devices have been extensively developed for behavioral neuroscience research to study neural correlations related to the behaviors of awake behaving animals, with an increasing focus on using small animals, such as rodents, to study complex behaviors. Therefore, collecting neural data from freely moving rodents is intriguing for a wide range of studies including neural processing changes with different behaviors (*67*), decision-making (*68*), social interactions (*18*), and movement-related diseases like PD (*69*), as they reflect specific physiological information. For example, the medial prefrontal cortex (mPFC) plays a crucial role in social interactions, such as the food competition test. In the test, by measuring mPFC neural activities, 18 different behavioral patterns were identified. In addition, symptoms of PD are accompanied by various neural activities, such as changes in the basal ganglia and synchronization of beta activity. In both scenarios, enabling natural movements in small animal models without human interaction or nonbiological electronic systems that can alter natural behavior is necessary for precise neural analysis. This printable, power-integrated neural recording system further suggests its extensibility for various implantable bioelectronics and behavioral neuroscience research, along with its potential for notably advanced understanding of the brain and its functions.

MATERIALS AND METHODS

Preparation of electrode inks for ZIMBs

To fabricate the cathode inks, α-MnO_2 active powders were prepared using the previously reported synthetic procedure (*70*). Briefly, 0.003 M $MnSO_4{\cdot}H_2O$ (Sigma-Aldrich) and 20 ml of 0.5 M H_2SO_4 (Samchun Co.) were added to 90 ml of deionized (DI) water and stirred until a clear solution was obtained. Subsequently, 20 ml of 0.1 M $KMnO_4$ (Sigma-Aldrich) aqueous solution was gradually added to the as-prepared solution, after which the solution was transferred to a Teflon-lined autoclave and heated at 120°C for 12 hours. Thereafter, the solution was cooled, subjected to centrifugation to collect the resulting materials, washed several times with DI water, and vacuum-dried at room temperature to obtain the α-MnO_2 active powders. The cathode ink for the nonplanar 3D printing was prepared by mixing the obtained α-MnO_2 powders, SWCNT, CNF suspension (solid content = 2 wt %, Sugino), and TOCN suspension (solid content = 1 wt %, University of Maine) using a planetary mixer (ARE-310, Thinky) with a composition ratio of α-MnO_2/SWCNT/CNF/TOCN = 80/10/5/5 (w/w/w/w). The control cathode ink was prepared by mixing α-MnO_2 powders, SWCNT, and PVDF dissolved in NMP with a composition ratio of α-MnO_2/SWCNT/PVDF = 80/10/10 (w/w/w). The Zn anode ink was prepared by mixing Zn powders (average diameter < 10 μm, Sigma-Aldrich), SWCNT, CNF suspension (solid content = 2 wt %), and TOCN suspension (solid content = 1 wt %, University of Maine) using a planetary mixer (ARE-310, Thinky) at a composition ratio of Zn/SWCNT/CNF/TOCN = 94/3/1.5/1.5 (w/w/w/w). The control anode ink was prepared by mixing Zn powders, SWCNT, and PVDF with a composition ratio of Zn/SWCNT/PVDF = 94/3/3 (w/w/w).

Preparation of quasi–solid-state gel composite electrolyte and packaging inks for ZIMBs

Before fabricating the gel composite electrolyte ink, the water-soluble photo-initiator [methylated β-cyclodextrin/2-hydroxy-2-methylpropiophenone (MCD-HMPP)] was prepared using the previously reported synthetic procedure (*71*). Briefly, 1.74 g (1.3 mmol) of MCD (Sigma-Aldrich) was dissolved in 6 ml of water, after which 0.2 ml (1.3 mmol) of HMPP (Sigma-Aldrich) was added. The colorless dispersion was sonicated for 5 min to yield a clear colorless solution. After undergoing solvent evaporation, the solid complex was vacuum-dried overnight. The MCD complexation enabled the dissolution of the HMPP photo-initiator in water. The gel composite electrolyte ink was prepared by mixing the gel electrolyte precursor solution and SiO_2 nanoparticles (average diameter, ~40 nm, Denka, Japan), which were used as a rheology-tuning agent. First, the gel electrolyte precursor solution was prepared by mixing 2 M $ZnSO_4$ + 0.2 M $MnSO_4$ aqueous liquid electrolyte, acrylamide (Sigma-Aldrich) monomer, *N*,*N*′-methylenebis(acrylamide) (MBA; Sigma-Aldrich) cross-linker, and MCD-HMPP photo-initiator. The composition ratio of the aqueous electrolyte/acrylamide/MBA was 99:10:1 (w/w/w), and that of the MCD-HMPP (relative to the acrylamide monomer) was 1 wt %. Subsequently, the SiO_2 nanoparticles were added to the gel electrolyte precursor solution and mixed using a planetary mixer (ARE-310, Thinky), in which the composition ratio of the gel electrolyte precursor solution/SiO_2 was 80:20 (w/w). The packaging ink was prepared by mixing a UV-curable resin (NOA68T, Norland Products Inc.) and SiO_2 nanoparticles with a composition ratio of resin/SiO_2 = 85:15 (w/w).

Nonplanar 3D printing and characterization of the ZIMB components

To demonstrate the 3D printability and conformability of the ZIMB components on nonplanar surfaces, the ramp and hemisphere-shaped 3D substrates were fabricated using a commercial fused deposition modeling (FDM)–type 3D printer (Almond, Opencreators) with polylactic acid filaments. The cathode and anode were fabricated using a DIW-based nonplanar 3D printing system (Image Master 350PC Smart, Musashi Engineering Inc.) consisting of a nozzle (inner diameter = 200 μm) connected to an ink-containing syringe, which was extruded by a pneumatic pressure controller according to a computer-aided design (CAD)–based predesign. As a control sample, planar electrodes were fabricated by printing the same cathode and anode inks on a PET film. The FEA was conducted using a commercial software Autodesk Inventor (Autodesk Inc.). The interactions of the SWCNT and TOCN were analyzed using a Raman spectrometer (LabRam Aramis, Horiba Jobin Yvon). The zeta potential of the electrode inks was examined using a Zetasizer (Nano ZS, Malvern Panalytical). The rheological properties of the cathode, anode, gel composite electrolyte, and packaging inks were investigated using a rheometer (MCR 302, Anton Paar). The UV curing reaction of the gel composite electrolyte was examined using an FTIR spectrometer (Alpha Platinum ATR, Bruker) with a spectral resolution of 4 cm^{-1}. The physical appearances and line widths of the printed electrodes (cathodes and anodes) were characterized using an optical microscope (LV100ND, Nikon). The surface and cross-sectional morphologies of the samples were examined by SEM (S4800, Hitachi) and energy-dispersive x-ray spectrometry (Ultim Max 65, Oxford Instruments) elemental mapping measurements.

Fabrication and characterization of ZIMBs for cranium electronics

To fabricate the ZIMB, first, the cranium of a mouse was scanned using a micro-CT (Skyscan 1176, Bruker) to obtain the computational 3D-rendered model of the cranium. The cranium model was fabricated using a commercial selective laser sintering (SLS)–type

3D printer (sPro60 SLS Center, 3D Systems). The UV-curable resin packaging/substrate of the ZIMB was 3D-printed on the nonplanar surface of the 3D-printed cranium model, after which the substrate was fully cured by UV irradiation (Hg UV lamp, peak intensity = 5000 mW cm^{-2}, Lichtzen) for 1 min. To pattern the gold (Au) current collector via metal sputtering, polyvinyl alcohol [PVA; weight-average molecular weight (M_w) = 9000 to 10,000, Sigma-Aldrich] masks were fabricated by printing the PVA ink. The PVA ink was prepared by mixing PVA aqueous solution (solid content = 30 wt %) and SiO_2 particles at a composition ratio of PVA aqueous solution/SiO_2 = 70:30 (w/w). The PVA ink was printed on the UV-cured resin substrate in an interdigitated pattern and dried at 60°C overnight. The deposition of Au on the mask-patterned resin substrate was performed using a direct current (DC) magnetron sputtering–based physical vapor deposition system (Infovion Inc.) in argon (Ar) gas with a power of 300 W for 5 min. The Au-deposited substrate was immersed in water to induce the dissolution and delamination of the PVA mask from the UV-cured resin substrate. Subsequently, the cathode ink, anode ink, and gel composite electrolyte inks were sequentially printed using the DIW-based nonplanar 3D-printing system. The printed cathode and anode were vacuum-dried at 50°C for 24 hours. Thereafter, the gel composite electrolyte ink was printed on the electrodes (cathode and anode) and then UV-cured to solidify the electrolyte. Last, the resin packaging ink was 3D-printed on the as-prepared gel composite electrolyte and subjected to UV curing for 1 min, resulting in a solidified, fully insulated battery encapsulation with a thickness of 57 μm. To fabricate a control pouch-type ZIMB, a cathode was prepared by blade casting the same cathode ink of the aforementioned ZIMB on a titanium (Ti) foil and vacuum-dried at 50°C for 24 hours. Then, the obtained cathode was assembled with a Zn foil anode, a glass fiber separator, and aqueous electrolyte (2 M $ZnSO_4$ + 0.2 M $MnSO_4$) and finally sealed with an aluminum (Al) pouch film as a packaging substance. The CV analysis of the cranium-customized ZIMB was conducted at a voltage range of 3.0 to 5.4 V and a scan rate of 0.2 mV s^{-1}. The CV analysis of the cranium-customized ZIMBs was performed using a potentiostat/galvanostat (VMP-300, Bio-Logic). The galvanostatic charge/discharge measurement was performed using a cycle tester (PNE Solution Co. Ltd) at ambient temperature.

Direct printing of liquid metals

A nozzle with an inner diameter of 5 μm was prepared by pulling a glass capillary (Sutter Instrument) with an inner diameter of 0.5 mm and an outer diameter of 1.0 mm using a pipette puller (P-1000, Sutter Instrument). The ink used for the liquid metal was eutectic gallium-indium alloy, EGaIn (75.5% gallium, 24.5% indium alloy by weight; Changsha Santech Materials Co. Ltd.). The EGaIn printing process was monitored using a microscope camera (QImaging Micropublisher 5.0 RTV, Teledyne Photometrics) to accurately manage the position of the nozzle relative to the substrate using a six-axis stage (H-820 6-Axis Hexapod, Physik Instrumente). In the case of 5-μm-diameter nozzle, the air pressure of 55 psi was applied to pull the EGaIn from the syringe to the tip of the glass capillary nozzle before starting printing with the velocity of 0.05 mm s^{-1}.

Fabrication of soft neural probes using liquid metal printing

The process of fabricating the soft neural probes involved the following steps: (i) A Si wafer was coated with a sacrificial layer of LOR 3A lift-off resist (MicroChem) using a spin coater. (ii) A parylene-C layer with a thickness of 1 μm was deposited on the sacrificial layer–coated Si wafer for the bottom passivation layer using a parylene coater. (iii) EGaIn was printed with 5-μm-width lines on this parylene-C layer. (iv) Another parylene-C layer with a thickness of 1.5 μm was deposited for the top passivation layer. (v) The photoresist S1818 (MicroChem) was spin-coated and then patterned using photolithography for defining the probe shape. (vi) The areas of parylene-C that were not covered by the S1818 layer were etched via O_2 plasma using a reactive ion etching system, and the S1818 photoresist was removed by acetone. (vii) The S1818 photoresist was spin-coated again and then patterned using photolithography for opening the electrode pads, and step (vi) was repeated. (viii) The resulting probes were lifted off from the Si wafer by dissolving the sacrificial layer with a remover PG solution (MicroChem). (ix) The released neural probes were then rinsed with DI water.

Electrodeposition of platinum nanoclusters

For preparing 25 ml of an electroplating solution, 25 ml of DI water, 5 mg of lead acetate trihydrate (Sigma-Aldrich), and 0.25 g of platinum tetrachloride (Sigma-Aldrich) were mixed at room temperature. The solution was then stirred using ultrasonic vibration for 20 min and filtered to remove impurities. Then, the electroplating was conducted by transferring ions between the cathode (a soft neural probe requiring electroplating) and the anode (a Pt electrode). Both the cathode and anode were immersed in the electroplating solution and connected to a source meter (Keithley 2400, Tektronix). The electroplating reaction occurred under an electrical voltage of 5 V and a compliance current of 0.1 mA for a duration of 60 s.

Electromechanical characterization

Pressing and releasing test

The PtB/EGaIn line was printed on a silicon wafer, followed by encapsulation with a parylene-C layer. Under conditions of pressing and releasing, using the lateral surface of a 0.5-mm-thick silicon wafer attached to a compression tester machine (Mark-10), the resistance change of the printed PtB/EGaIn was measured by connecting both ends to a source meter (Keithley 4200-SCS, Tektronix).

Stretching and self-healing test

The sample fracturing for stretching and the self-healing test was induced using a step motor controller (SMC-100, Ecopia) and a uniaxial stretching stage. The PtB/EGaIn line printed on a parylene-C–coated poly(dimethylsiloxane) film was affixed to the stretching stage and stretched to 250%. Then, the resistance change of the printed PtB/EGaIn was measured by connecting both ends to a source meter (Keithley 4200-SCS, Tektronix). The movement of the stretching stage was controlled by a high-speed motion controller (PMC-1HS program, Autonics). The resistance change of the PtB/EGaIn sample was constantly measured during the self-healing process at a sampling rate of 5 ms.

Impedance spectroscopy

The pristine EGaIn and PtB/EGaIn probes were tested for impedance measurements in a PBS solution (Sigma-Aldrich). For the in vivo impedance measurement, a reference electrode and PtB/EGaIn probes were implanted into the brain of an anesthetized, head-fixed mouse (C57BL/6N, male). All impedance measurements were conducted using a multichannel potentiostat (PMC-1000, AMETEK) at a frequency range of 0.01 to 100 kHz.

Tensile tests

The stress-strain characteristics of the pristine EGaIn and PtB/EGaIn were used to measure their elastic modulus during a tensile test using a TXATM micro-precision texture analyzer (Yeonjin S-Tech, Republic of Korea). The stretching and releasing of the samples were conducted at a strain rate of 10 μm s^{-1}.

Animal experiments

The mice used in the study were 8-week-old male C57BL/6N mice and were housed in a controlled environment with a temperature of 23°C, humidity of 50%, and a 12-hour light/12-hour dark cycle. For anesthetizing, a mixture of 20 μl of xylazine, 80 μl of ketamine, and 100 μl PBS was used per mouse. All animal experiments were conducted in compliance with the guidelines provided in the *Guide for the Care and Use of Laboratory Animals* of the Yonsei University Institutional Animal Care and Use Committee. The protocols were approved by the Committee on the Ethics of Animal Experiments of Yonsei University (approval number IACUC-A-202201-1411-02).

Open field test

Open field test was performed in a 2100 cm^2 square arena. The arena was cleaned with 70% ethanol between testing trials. Normal and cranium system–implanted mice were housed in a controlled environment with a temperature of 23°C, a humidity of 50%, and a 12-hour light/12-hour dark cycle. For testing, C57BL/6N normal mice or cranium system–implanted mice ($n = 5$ per group) were placed in the center of the open field and allowed to move freely for 5 min. Movements were video-recorded and analyzed by using an ANY-maze software (version 4.3; Stoelting Co., Wood Dale, IL). Time in the center zone was the primary measure of anxiety-like behaviors. Specifically, the center was defined as a square comprising 50% of the total area of the open field arena.

Thermal characterization

For the thermal characterization during in vivo tests, cranium system–implanted C57BL/6N mice were anesthetized and fixed on a rodent adaptor composed of jaw cuff and ear bars (RWD Life Science, USA). The temperature was measured by IR camera (T650sc, FLIR Systems), and the temperature distribution of the images and video was analyzed using FLIR ResearchIR software (ResearchIR Max, FLIR Systems).

Wireless neural recording

To analyze the data from LFPs and single-unit potentials, a wireless neural recording system was used. This system included a lightweight wireless recording device designed for mice (JAGA penny) and NeuroPhys/NeuroSorter software (JAGA Systems, Jiang-hi). A sampling rate of 20,360 Hz and 60-Hz notch filter were used during the recording. Band-pass filters ranging (i) from 0.1 to 300 Hz and (ii) from 300 to 3000 Hz were used to record LFPs and single-unit spikes, respectively.

Simultaneous recordings of signals from each of the four locations were conducted for both the LFPs and single-unit traces. These signals were subsequently plotted together to facilitate a comprehensive analysis and comparison of the data obtained from each location. The soft neural probes were surgically implanted into predrilled specific stereotaxic coordinates within the brain of an anesthetized mouse (C57BL/6N, male), and the set screw (stainless steel) size of 0 to 80 (according to Unified National Fine) was used for a reference electrode. This implantation procedure was facilitated by a six-axis movement stage. To ensure reliability and validity, each experiment was conducted with at least three different mice. Stereotaxic coordinates: (i) Motor cortices (MO): 2 mm AP, 2 mm ML, 1.5 mm DV from bregma; 2 mm AP, 1 mm ML, 1.5 mm DV; 2 mm AP, −1 mm ML, 1.5 mm DV; 2 mm AP, −2 mm ML, 1.5 mm DV; 1 mm AP, 1 mm ML, 1.5 mm DV; 1 mm AP, −1 mm ML, 1.5 mm DV; 0.5 mm AP, 1.5 mm ML, 1.0 mm DV; 0.5 mm AP, −1.5 mm ML, 1.5 mm DV. (ii) Hippocampal regions (HIP): −1 mm AP, 2 mm ML, 1.5 mm DV; −1 mm AP, 1 mm ML, 1.5 mm DV; −1 mm AP, −1 mm ML, 1.5 mm DV; −1 mm AP, −2 mm ML, 1.5 mm DV; −2 mm AP, 2.5 mm ML, 1.5 mm DV; −2 mm AP, 1.5 mm ML, 1.5 mm DV; −2 mm AP, −1.5 mm ML, 1.5 mm DV; −2 mm AP, −2.5 mm ML, 1.5 mm DV. (iii) Reference: 2.5 mm AP, 1 mm ML. AP, ML, and DV represent anteroposterior, mediolateral, and dorsoventral, respectively.

Immunohistochemistry

Mice brains were fixed with 4% paraformaldehyde for 24 hours and transferred to 30% sucrose for 3 days. Brains were cut into 30-μm axial sections using a freezing microtome. The sections were incubated in blocking solution (PBS, 5% normal goat serum, and 0.2% Triton X-100) for 1 hour at room temperature and incubated with primary antibodies in blocking solution overnight at 4°C. The primary antibodies used were as follows: FOX3 (NeuN) (BioLegend, 834502, 1:300), Iba-1 (Invitrogen, 1:200), and GFAP (Invitrogen, 1:300). After the primary immunoreaction, sections were incubated with Alexa Fluor 488 (Invitrogen, A-21202, 1:500)–, Alexa Fluor 594 (Invitrogen, A-21209, 1:500)–, and Alexa Fluor 647 (Invitrogen, A32733, 1:500)–conjugated secondary antibodies. Immunostaining of the sections was visualized using an Axio Imager M2 (Carl Zeiss) fluorescence microscope.

Data analysis

Spike detection and PCA clustering

All analyses of wireless neural recording data were conducted using MATLAB with the four open-source toolboxes (Statistics and Machine Signal Processing Toolbox, Learning Toolbox, Circular Statistics Toolbox, Bioinformatics Toolbox by Philipp Berens). The spike detection threshold was set as −5 times the SD of the filtered time series, which was band pass–filtered between 300 and 3000 Hz. PCA was used to reduce the dimensionality of the data using the *k*-means function.

LFP signal filtering

All analyses of wireless neural recording data were conducted using MATLAB with an open-source toolbox (Signal Processing Toolbox). The signals were band pass–filtered by second-order Butterworth filter with beta (10 to 45 Hz) and theta (6 to 10 Hz) frequency range.

LFP power spectrogram

All analyses of wireless neural recording data were done using MATLAB with an open-source toolbox (Signal Processing Toolbox). The unfiltered LFPs were low pass–filtered by fourth-order Butterworth filter with the cutoff frequency value of 300 Hz. For the analysis, signals were downsampled from the original sampling rate of 20,360 Hz to 1 kHz. Spectrogram of short-time Fourier transform (STFT) was done using the Hanning windows of size 500 samples, with 50% samples overlapping between adjoining windows. In each window, a discrete Fourier transform was calculated with 2048 × 4 sampling points. The resulting STFT amplitudes were normalized

by subtracting the baseline and again dividing by the baseline, where the baseline is the mean absolute STFT amplitude from 10 to 20 s. The spectrograms were drawn also using the open-source toolbox (Image Processing Toolbox). To draw the spectrogram in a continuous color scale, normalized STFT amplitudes were convolution-filtered using the 2D average filter with the filter size 2×16.

Calculation of L ratio

The L ratio was calculated on the basis of the Mahalanobis distance as below

$$L_{\text{ratio}} = \frac{L(C)}{N(C)} = \frac{\sum_{i \notin C} 1 - CDF_{\chi^2}(MD_{i,c}{}^2)}{N_c}$$

In the given context, N_c is the number of spikes in cluster C, $i \notin C$ is the set of spikes that are not members of the cluster C, $CDF_{\chi}{}^2$ presents the cumulative distribution function of the χ^2 distribution in an 8D feature space, and $MD_{i,c}{}^2$ is the Mahalanobis distance of spike i from C. In particular, an L ratio of less than 0.05 indicates good separation and isolation of the cluster.

Statistical analysis

All data were presented as means ± SD. Statistic calculations of P value were performed using a customized code of MATLAB.

Supplementary Materials

This PDF file includes:

Figs. S1 to S40
Legends for movies S1 to S6
References

Other Supplementary Material for this manuscript includes the following:

Movies S1 to S6

REFERENCES AND NOTES

1. I. Chiaradia, M. A. Lancaster, Brain organoids for the study of human neurobiology at the interface of in vitro and in vivo. *Nat. Neurosci.* **23**, 1496–1508 (2020).
2. S. M. Won, E. Song, J. T. Reeder, J. A. Rogers, Emerging modalities and implantable technologies for neuromodulation. *Cell* **181**, 115–135 (2020).
3. M. Lee, H. J. Shim, C. Choi, D.-H. Kim, Soft high-resolution neural interfacing probes: Materials and design approaches. *Nano Lett.* **19**, 2741–2749 (2019).
4. S. P. Lacour, G. Courtine, J. Guck, Materials and technologies for soft implantable neuroprostheses. *Nat. Rev. Mater.* **1**, 16063 (2016).
5. A. E. Urai, B. Doiron, A. M. Leifer, A. K. Churchland, Large-scale neural recordings call for new insights to link brain and behavior. *Nat. Neurosci.* **25**, 11–19 (2022).
6. J. J. Jun, N. A. Steinmetz, J. H. Siegle, D. J. Denman, M. Bauza, B. Barbarits, A. K. Lee, C. A. Anastassiou, A. Andrei, Ç. Aydın, M. Barbic, T. J. Blanche, V. Bonin, J. Couto, B. Dutta, S. L. Gratiy, D. A. Gutnisky, M. Häusser, B. Karsh, P. Ledochowitsch, C. M. Lopez, C. Mitelut, S. Musa, M. Okun, M. Pachitariu, J. Putzeys, P. D. Rich, C. Rossant, W. Sun, K. Svoboda, M. Carandini, K. D. Harris, C. Koch, J. O'Keefe, T. D. Harris, Fully integrated silicon probes for high-density recording of neural activity. *Nature* **551**, 232–236 (2017).
7. D. Khodagholy, J. N. Gelinas, T. Thesen, W. Doyle, O. Devinsky, G. G. Malliaras, G. Buzsáki, NeuroGrid: Recording action potentials from the surface of the brain. *Nat. Neurosci.* **18**, 310–315 (2015).
8. T. D. Y. Kozai, N. B. Langhals, P. R. Patel, X. Deng, H. Zhang, K. L. Smith, J. Lahann, N. A. Kotov, D. R. Kipke, Ultrasmall implantable composite microelectrodes with bioactive surfaces for chronic neural interfaces. *Nat. Mater.* **11**, 1065–1073 (2012).
9. S. I. Park, D. S. Brenner, G. Shin, C. D. Morgan, B. A. Copits, H. U. Chung, M. Y. Pullen, K. N. Noh, S. Davidson, S. J. Oh, J. Yoon, K.-I. Jang, V. K. Samineni, M. Norman, J. G. Grajales-Reyes, S. K. Vogt, S. S. Sundaram, K. M. Wilson, J. S. Ha, R. Xu, T. Pan, T. Kim, Y. Huang, M. C. Montana, J. P. Golden, M. R. Bruchas, R. W. Gereau IV, J. A. Rogers, Soft, stretchable, fully implantable miniaturized optoelectronic systems for wireless optogenetics. *Nat. Biotechnol.* **33**, 1280–1286 (2015).
10. J. Liu, T.-M. Fu, Z. Cheng, G. Hong, T. Zhou, L. Jin, M. Duvvuri, Z. Jiang, P. Kruskal, C. Xie, Z. Suo, Y. Fang, C. M. Lieber, Syringe-injectable electronics. *Nat. Nanotechnol.* **10**, 629–636 (2015).
11. X. Yang, T. Zhou, T. J. Zwang, G. Hong, Y. Zhao, R. D. Viveros, T.-M. Fu, T. Gao, C. M. Lieber, Bioinspired neuron-like electronics. *Nat. Mater.* **18**, 510–517 (2019).
12. T. G. Schuhmann Jr., J. Yao, G. Hong, T.-M. Fu, C. M. Lieber, Syringe-injectable electronics with a plug-and-play input/output interface. *Nano Lett.* **17**, 5836–5842 (2017).
13. R. Milton, N. Shahidi, V. Dragoi, Dynamic states of population activity in prefrontal cortical networks of freely-moving macaque. *Nat. Commun.* **11**, 1948 (2020).
14. V. Marx, Neuroscientists go wireless. *Nat. Methods* **18**, 1150–1154 (2021).
15. J. Ausra, S. J. Munger, A. Azami, A. Burton, R. Peralta, J. E. Miller, P. Gutruf, Wireless battery free fully implantable multimodal recording and neuromodulation tools for songbirds. *Nat. Commun.* **12**, 1968 (2021).
16. S. M. Won, L. Cai, P. Gutruf, J. A. Rogers, Wireless and battery-free technologies for neuroengineering. *Nat. Biomed. Eng.* **7**, 405–423 (2023).
17. C. Y. Kim, M. J. Ku, R. Qazi, H. J. Nam, J. W. Park, K. S. Nam, S. Oh, I. Kang, J.-H. Jang, W. Y. Kim, J.-H. Kim, J.-W. Jeong, Soft subdermal implant capable of wireless battery charging and programmable controls for applications in optogenetics. *Nat. Commun.* **12**, 535 (2021).
18. H. Shin, J. Byun, D. Roh, N. Choi, H.-S. Shin, I.-J. Cho, Interference-free, lightweight wireless neural probe system for investigating brain activity during natural competition. *Biosens. Bioelectron.* **195**, 113665 (2022).
19. J. Lee, V. Leung, A.-H. Lee, J. Huang, P. Asbeck, P. P. Mercier, S. Shellhammer, L. Larson, F. Laiwalla, A. Nurmikko, Neural recording and stimulation using wireless networks of microimplants. *Nat. Electron.* **4**, 604–614 (2021).
20. S. Idogawa, K. Yamashita, R. Sanda, R. Numano, K. Koida, T. Kawano, A lightweight, wireless Bluetooth-low-energy neuronal recording system for mice. *Sens. Actuators B Chem.* **331**, 129423 (2021).
21. A. Zhou, S. R. Santacruz, B. C. Johnson, G. Alexandrov, A. Moin, F. L. Burghardt, J. M. Rabaey, J. M. Carmena, R. Muller, A wireless and artefact-free 128-channel neuromodulation device for closed-loop stimulation and recording in non-human primates. *Nat. Biomed. Eng.* **3**, 15–26 (2019).
22. D. A. Schwarz, M. A. Lebedev, T. L. Hanson, D. F. Dimitrov, G. Lehew, J. Meloy, S. Rajangam, V. Subramanian, P. J. Ifft, Z. Li, A. Ramakrishnan, A. Tate, K. Z. Zhuang, M. A. L. Nicolelis, Chronic, wireless recordings of large-scale brain activity in freely moving rhesus monkeys. *Nat. Methods* **11**, 670–676 (2014).
23. A. Burton, S. M. Won, A. K. Sohrabi, T. Stuart, A. Amirhossein, J. U. Kim, Y. Park, A. Gabros, J. A. Rogers, F. Vitale, A. G. Richardson, P. Gutruf, Wireless, battery-free, and fully implantable electrical neurostimulation in freely moving rodents. *Microsyst. Nanoeng.* **7**, 62 (2021).
24. L. Melo-Thomas, K.-A. Engelhardt, U. Thomas, D. Hoehl, S. Thomas, M. Wöhr, B. Werner, F. Bremmer, R. K. W. Schwarting, A wireless, bidirectional interface for in vivo recording and stimulation of neural activity in freely behaving rats. *J. Vis. Exp.*, e56299 (2017).
25. T. Hasegawa, H. Fujimoto, K. Tashiro, M. Nonomura, A. Tsuchiya, D. Watanabe, A wireless neural recording system with a precision motorized microdrive for freely behaving animals. *Sci. Rep.* **5**, 7853 (2015).
26. M. D. Dickey, Stretchable and soft electronics using liquid metals. *Adv. Mater.* **29**, 1606425 (2017).
27. Y.-G. Park, G.-Y. Lee, J. Jang, S. M. Yun, E. Kim, J.-U. Park, Liquid metal-based soft electronics for wearable healthcare. *Adv. Healthc. Mater.* **10**, e2002280 (2021).
28. C. Guo, Y. Yu, J. Liu, Rapidly patterning conductive components on skin substrates as physiological testing devices via liquid metal spraying and pre-designed mask. *J. Mater. Chem. B* **2**, 5739–5745 (2014).
29. Y.-G. Park, H. S. An, J.-Y. Kim, J.-U. Park, High-resolution, reconfigurable printing of liquid metals with three-dimensional structures. *Sci. Adv.* **5**, eaaw2844 (2019).
30. Y. Wu, M. Wu, A. Vázquez-Guardado, J. Kim, X. Zhang, R. Avila, J.-T. Kim, Y. Deng, Y. Yu, S. Melzer, Y. Bai, H. Yoon, L. Meng, Y. Zhang, H. Guo, L. Hong, E. E. Kanatzidis, C. R. Haney, E. A. Waters, A. R. Banks, Z. Hu, F. Lie, L. P. Chamorro, B. L. Sabatini, Y. Huang, Y. Kozorovitskiy, J. A. Rogers, Wireless multi-lateral optofluidic microsystems for real-time programmable optogenetics and photopharmacology. *Nat. Commun.* **13**, 5571 (2022).
31. H. Zhang, P. Gutruf, K. Meacham, M. C. Montana, X. Zhao, A. M. Chiarelli, A. Vázquez-Guardado, A. Norris, L. Lu, Q. Guo, C. Xu, Y. Wu, H. Zhao, X. Ning, W. Bai, I. Kandela, C. R. Haney, D. Chanda, R. W. Gereau, J. A. Rogers, Wireless, battery-free optoelectronic systems as subdermal implants for local tissue oximetry. *Sci. Adv.* **5**, eaaw0873 (2019).
32. H. Li, C. Han, Y. Huang, Y. Huang, M. Zhu, Z. Pei, Q. Xue, Z. Wang, Z. Liu, Z. Tang, Y. Wang, F. Kang, B. Li, C. Zhi, An extremely safe and wearable solid-state zinc ion battery based on a hierarchical structured polymer electrolyte. *Energy Environ. Sci.* **11**, 941–951 (2018).
33. D. Kim, D. Kim, H. Lee, Y. R. Jeong, S.-J. Lee, G. Yang, H. Kim, G. Lee, S. Jeon, G. Zi, J. Kim, J. S. Ha, Body-attachable and stretchable multisensors integrated with wirelessly rechargeable energy storage devices. *Adv. Mater.* **28**, 748–756 (2016).
34. Y. Lim, J. Yoon, J. Yun, D. Kim, S. Y. Hong, S.-J. Lee, G. Zi, J. S. Ha, Biaxially stretchable, integrated array of high performance microsupercapacitors. *ACS Nano* **8**, 11639–11650 (2014).
35. N. Kim, J. Kim, J. Seo, C. Hong, J. Lee, Stretchable inorganic LED displays with double-layer modular design for high fill factor. *ACS Appl. Mater. Interfaces* **14**, 4344–4351 (2022).

36. M.-C. Li, Q. Wu, R. J. Moon, M. A. Hubbe, M. J. Bortner, Rheological aspects of cellulose nanomaterials: Governing factors and emerging applications. *Adv. Mater.* **33**, e2006052 (2021).
37. Y. Li, H. Zhu, Y. Wang, U. Ray, S. Zhu, J. Dai, C. Chen, K. Fu, S.-H. Jang, D. Henderson, T. Li, L. Hu, Cellulose-nanofiber-enabled 3d printing of a carbon-nanotube microfiber network. *Small Methods* **1**, 1700222 (2017).
38. Y. Li, H. Zhu, F. Shen, J. Wan, S. Lacey, Z. Fang, H. Dai, L. Hu, Nanocellulose as green dispersant for two-dimensional energy materials. *Nano Energy* **13**, 346–354 (2015).
39. Y. Kuang, C. Chen, G. Pastel, Y. Li, J. Song, R. Mi, W. Kong, B. Liu, Y. Jiang, K. Yang, L. Hu, Conductive cellulose nanofiber enabled thick electrode for compact and flexible energy storage devices. *Adv. Energy Mater.* **8**, 1802398 (2018).
40. J. Jiang, G. Oberdörster, P. Biswas, Characterization of size, surface charge, and agglomeration state of nanoparticle dispersions for toxicological studies. *J. Nanopart. Res.* **11**, 77–89 (2009).
41. S. Bhattacharjee, DLS and zeta potential—What they are and what they are not? *J. Control. Release* **235**, 337–351 (2016).
42. M. Gopu, S. Rathod, U. Namangalam, R. K. Pujala, S. S. Kumar, D. Mampallil, Evaporation of inclined drops: Formation of asymmetric ring patterns. *Langmuir* **36**, 8137–8143 (2020).
43. B. F. Winhard, S. Haugg, R. Blick, G. A. Schneider, K. P. Furlan, Direct writing of colloidal suspensions onto inclined surfaces: Optimizing dispense volume for homogeneous structures. *J. Colloid Interface Sci.* **597**, 137–148 (2021).
44. F. Matter, A. L. Luna, M. Niederberger, From colloidal dispersions to aerogels: How to master nanoparticle gelation. *Nano Today* **30**, 100827 (2020).
45. S.-H. Kim, K.-H. Choi, S.-J. Cho, J. Yoo, S.-S. Lee, S.-Y. Lee, Flexible/shape-versatile, bipolar all-solid-state lithium-ion batteries prepared by multistage printing. *Energy Environ. Sci.* **11**, 321–330 (2018).
46. S.-H. Kim, J.-H. Kim, S.-J. Cho, S.-Y. Lee, All-solid-state printed bipolar Li–S batteries. *Adv. Energy Mater.* **9**, 1901841 (2019).
47. S.-H. Kim, J.-M. Kim, D. B. Ahn, S.-Y. Lee, Cellulose nanofiber/carbon nanotube-based bicontinuous ion/electron conduction networks for high-performance aqueous Zn-ion batteries. *Small* **16**, e2002837 (2020).
48. H.-D. Um, K.-H. Choi, I. Hwang, S.-H. Kim, K. Seo, S.-Y. Lee, Monolithically integrated, photo-rechargeable portable power sources based on miniaturized Si solar cells and printed solid-state lithium-ion batteries. *Energy Environ. Sci.* **10**, 931–940 (2017).
49. P. Sun, X. Li, J. Shao, P. V. Braun, High-performance packaged 3d lithium-ion microbatteries fabricated using imprint lithography. *Adv. Mater.* **33**, 2006229 (2021).
50. T.-S. Wei, B. Y. Ahn, J. Grotto, J. A. Lewis, 3D printing of customized li-ion batteries with thick electrodes. *Adv. Mater.* **30**, e1703027 (2018).
51. L. Lu, P. Gutruf, L. Xia, D. L. Bhatti, X. Wang, A. Vazquez-Guardado, X. Ning, X. Shen, T. Sang, R. Ma, G. Pakeltis, G. Sobczak, H. Zhang, D. Seo, M. Xue, L. Yin, D. Chanda, X. Sheng, M. R. Bruchas, J. A. Rogers, Wireless optoelectronic photometers for monitoring neuronal dynamics in the deep brain. *Proc. Natl. Acad. Sci. U.S.A.* **115**, E1374–E1383 (2018).
52. C. Kathe, F. Michoud, P. Schönle, A. Rowald, N. Brun, J. Ravier, I. Furfaro, V. Paggi, K. Kim, S. Soloukey, L. Asboth, T. H. Hutson, I. Jelescu, A. Philippides, N. Alwahab, J. Gandar, D. Huber, C. I. De Zeeuw, Q. Barraud, Q. Huang, S. P. Lacour, G. Courtine, Wireless closed-loop optogenetics across the entire dorsoventral spinal cord in mice. *Nat. Biotechnol.* **40**, 198–208 (2022).
53. W. Sun, F. Wang, S. Hou, C. Yang, X. Fan, Z. Ma, T. Gao, F. Han, R. Hu, M. Zhu, C. Wang, Zn/MnO_2 battery chemistry with H^+ and Zn^{2+} coinsertion. *J. Am. Chem. Soc.* **139**, 9775–9778 (2017).
54. Y. Fu, Q. Wei, G. Zhang, X. Wang, J. Zhang, Y. Hu, D. Wang, L. Zuin, T. Zhou, Y. Wu, S. Sun, High-performance reversible aqueous Zn-ion battery based on porous MnO_x nanorods coated by MOF-derived N-doped carbon. *Adv. Energy Mater.* **8**, 1801445 (2018).
55. Q. Zhao, X. Chen, Z. Wang, L. Yang, R. Qin, J. Yang, Y. Song, S. Ding, M. Weng, W. Huang, J. Liu, W. Zhao, G. Qian, K. Yang, Y. Cui, H. Chen, F. Pan, Unravelling H^+/Zn^{2+} synergistic intercalation in a novel phase of manganese oxide for high-performance aqueous rechargeable battery. *Small* **15**, e1904545 (2019).
56. A. Wang, D. Jung, D. Lee, H. Wang, Impedance characterization and modeling of subcellular to micro-sized electrodes with varying materials and PEDOT: PSS coating for bioelectrical interfaces. *ACS Appl. Electron. Mater.* **3**, 5226–5239 (2021).
57. N. J. Michelson, A. L. Vazquez, J. R. Eles, J. W. Salatino, E. K. Purcell, J. J. Williams, X. T. Cui, T. D. Y. Kozai, Multi-scale, multi-modal analysis uncovers complex relationship at the brain tissue-implant neural interface: New emphasis on the biological interface. *J. Neural Eng.* **15**, 033001 (2018).
58. R. A. Nawrocki, Super- and ultrathin organic field-effect transistors: From flexibility to super- and ultraflexibility. *Adv. Funct. Mater.* **29**, 1906908 (2019).
59. S. Nimbalkar, E. Castagnola, A. Balasubramani, A. Scarpellini, S. Samejima, A. Khorasani, A. Boissenin, S. Thongpang, C. Moritz, S. Kassegne, Ultra-capacitive carbon neural probe allows simultaneous long-term electrical stimulations and high-resolution neurotransmitter detection. *Sci. Rep.* **8**, 6958 (2018).
60. R. Fiáth, A. L. Márton, F. Mátyás, D. Pinke, G. Márton, K. Tóth, I. Ulbert, Slow insertion of silicon probes improves the quality of acute neuronal recordings. *Sci. Rep.* **9**, 111 (2019).
61. J. D. Bailoo, M. O. Bohlen, D. Wahlsten, The precision of video and photocell tracking systems and the elimination of tracking errors with infrared backlighting. *J. Neurosci. Methods* **188**, 45–52 (2010).
62. S. Lei, Z. Liu, C. Liu, J. Li, B. Lu, S. Liang, J. Zhou, Opportunities for biocompatible and safe zinc-based batteries. *Energy Environ. Sci.* **15**, 4911–4927 (2022).
63. Z. Xu, O. Agbigbe, N. Nigro, G. Yakobi, J. Shapiro, Y. Ginosar, Use of high-resolution thermography as a validation measure to confirm epidural anesthesia in mice: A cross-over study. *Int. J. Obstet. Anesth.* **46**, 102981 (2021).
64. Z. Nosrati, M. Bergamo, C. Rodríguez-Rodríguez, K. Saatchi, U. O. Häfeli, Refinement and validation of infrared thermal imaging (IRT): A non-invasive technique to measure disease activity in a mouse model of rheumatoid arthritis. *Arthritis Res. Ther.* **22**, 281 (2020).
65. A. Suarez-Perez, G. Gabriel, B. Rebollo, X. Illa, A. Guimerà-Brunet, J. Hernández-Ferrer, M. T. Martínez, R. Villa, M. V. Sanchez-Vives, Quantification of signal-to-noise ratio in cerebral cortex recordings using flexible MEAs with co-localized platinum black, carbon nanotubes, and gold electrodes. *Front. Neurosci.* **12**, 862 (2018).
66. F. Fuhrmann, D. Justus, L. Sosulina, H. Kaneko, T. Beutel, D. Friedrichs, S. Schoch, M. K. Schwarz, M. Fuhrmann, S. Remy, Locomotion, theta oscillations, and the speed-correlated firing of hippocampal neurons are controlled by a medial septal glutamatergic circuit. *Neuron* **86**, 1253–1264 (2015).
67. H.-C. Shin, J. K. Chapin, Movement induced modulation of afferent transmission to single neurons in the ventroposterior thalamus and somatosensory cortex in rat. *Exp. Brain Res.* **81**, 515–522 (1990).
68. N. Uchida, Z. F. Mainen, Speed and accuracy of olfactory discrimination in the rat. *Nat. Neurosci.* **6**, 1224–1229 (2003).
69. M. Bočková, I. Rektor, Impairment of brain functions in Parkinson's disease reflected by alterations in neural connectivity in EEG studies: A viewpoint. *Clin. Neurophysiol.* **130**, 239–247 (2019).
70. H. Pan, Y. Shao, P. Yan, Y. Cheng, K. S. Han, Z. Nie, C. Wang, J. Yang, X. Li, P. Bhattacharya, K. T. Mueller, J. Liu, Reversible aqueous zinc/manganese oxide energy storage from conversion reactions. *Nat. Energy* **1**, 16039 (2016).
71. I. C. Alupei, V. Alupei, H. Ritter, Cyclodextrins in polymer synthesis: Photoinitiated free-radical polymerization of *N*-isopropylacrylamide in water initiated by a methylated β-cyclodextrin/2-hydroxy-2-methyl-1-phenylpropan-1-one host/guest complex. *Macromol. Rapid Commun.* **23**, 55–58 (2002).
72. C. P. Romero, R. I. Jeldres, G. R. Quezada, F. Concha, P. G. Toledo, Zeta potential and viscosity of colloidal silica suspensions: Effect of seawater salts, pH, flocculant, and shear rate. *Colloids Surf. A Physicochem. Eng. Asp.* **538**, 210–218 (2018).
73. H. Tsurusawa, M. Leocmach, J. Russo, H. Tanaka, Direct link between mechanical stability in gels and percolation of isostatic particles. *Sci. Adv.* **5**, eaav6090 (2019).

Acknowledgments

Funding: This work was supported by the Ministry of Science & ICT (MSIT); the Ministry of Trade, Industry and Energy (MOTIE); the Ministry of Health & Welfare; and the Ministry of Food and Drug Safety of Korea through the National Research Foundation (2021M3H4A1A02099355 and 2023R1A2C2006257), ERC Program (2022R1A5A6000846), and the Korea Medical Device Development Fund grant (RMS 2022-11-1209/KMDF RS-2022-00141392). This work was also supported by Institute for Basic Science (IBS-R026-D1). **Author contributions:** Y.W.K., D.B.A., and Y.-G.P. carried out the experiment, analyzed the data, and wrote the manuscript. C.S.K. and Y.-M.H. were involved in all animal experiments and the related analysis. E.K., D.H.L., S.-W.K., K.-H.L., and W.-Y.K. were involved in device fabrications. J.-U.P., S.-Y.L., J.W.C., and H.H.J. oversaw all of the research phases and revised the manuscript. All authors discussed and commented on the manuscript. **Competing interests:** The authors declare that they have no competing interests. **Data and materials availability:** All data needed to evaluate the conclusions in the paper are present in the paper and/or the Supplementary Materials. All codes are available at https://doi.org/10.5281/zenodo.10654840.

Submitted 6 December 2023
Accepted 27 February 2024
Published 3 April 2024
10.1126/sciadv.adn3784

ScienceAdvances

Power-integrated, wireless neural recording systems on the cranium using a direct printing method for deep-brain analysis

Yong Won Kwon, David B. Ahn, Young-Geun Park, Enji Kim, Dong Ha Lee, Sang-Woo Kim, Kwon-Hyung Lee, Won-Yeong Kim, Yeon-Mi Hong, Chin Su Koh, Hyun Ho Jung, Jin Woo Chang, Sang-Young Lee, and Jang-Ung Park

Sci. Adv. **10** (14), eadn3784. DOI: 10.1126/sciadv.adn3784

Science Advances (ISSN 2375-2548) is published by the American Association for the Advancement of Science. 1200 New York Avenue NW, Washington, DC 20005. The title *Science Advances* is a registered trademark of AAAS.